DEVELOPMENT OF COMPREHENSIVE NUMERICAL SCHEMES FOR PREDICTING EVAPORATING GAS-DROPLETS FLOW PROCESSES OF A LIQUID-FUELED COMBUSTOR

(NAG-092)

Semi-Annual Report

June 15, 1988 - November 30, 1988

by

C. P. Chen

Department of Mechanical Engineering
The University of Alabama in Huntsville
Huntsville, AL 35899

for

NASA - Marshall Space Flight Center

INTRODUCTION

The objective of this study is to develop a two- and three-dimensional comprehensive spray combustion computer simulation code to study the complex physical processes involved in a liquid-fueled combustor. Efforts of this study in the last six months include: (1) implementing the Stochastic/two-equation model for turbulent droplet dispersion calculation; (2) testing the transient particle tracking methodology in a benchmark flow field; (3) upgrading and test the two-equation k-E model for the ARICC code. In the following, progresses in these studies will be briefly described.

(1) Implementations of the Stochastic Lagrangian particle tracking model into the MAST code have been completed. We utilized the operator-splitting technique such that the two-way coupling between the two phases is accounted for in a multi-corrector procedure. This operator-splitting technique eliminate the global iteration processes used in the conventional SIMPL/PSIC (particle source in cell) method. This method is time-accurate, and has been shown to very efficient for transient spray calculations.

(2) Testing of the above mentioned two-phase methodology for single injector spray has been carried out. The testing conditions for the Horiyasu's experiment setups are shown in Table 1. At the injection exit, the distribution of droplet sizes is modeled by a X-square function. Particle/droplet interaction was modeled by random sampling from assumed probability distribution of flow turbulence. For the k-E model

used, this probability distribution is Gaussian. Figure 1 and 2 show the penetration of spray at different chamber pressures. Comparisons of the computed spray penetrations with experimental data are shown in Figure 3. The agreement is excellent and shows the time-accuracy capability of the current methodolgy. The efficiency assessment of the MAST calculations is summarized in Table 3. It can be seen that the MAST reduces CPU time by one order-of-magnitude and very much particle-number insensitive. The robustness of this methodology is demonstrated for this test case. Further testings are underway for hollow-cone sprays.

(3) Turbulence model upgrade for ARICC and the testing of the ARICC performance on benchmark turbulent flows have been completed. Due to the explicit ALE-ICE method used in the ARICC code, the inclusion of the k-E model highly reduced the time-step for marching solutions. The efficiency of the ARICC code with advanced turbulence models was seen to deteriorate significantly. Detailed implementation and validation studies can be found in Lee's Master Thesis which is funded by this grant and is enclosed as an appendix.

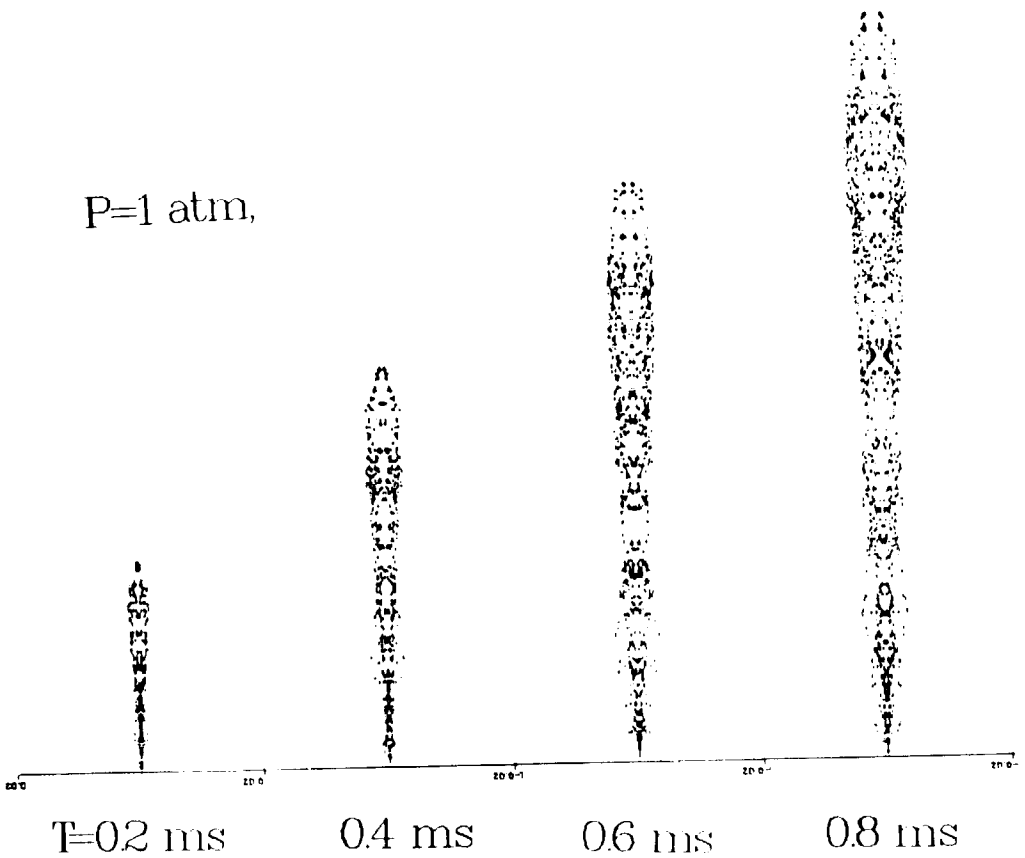

Figure 1. Single Orifice spray in 1 Atm Chamber

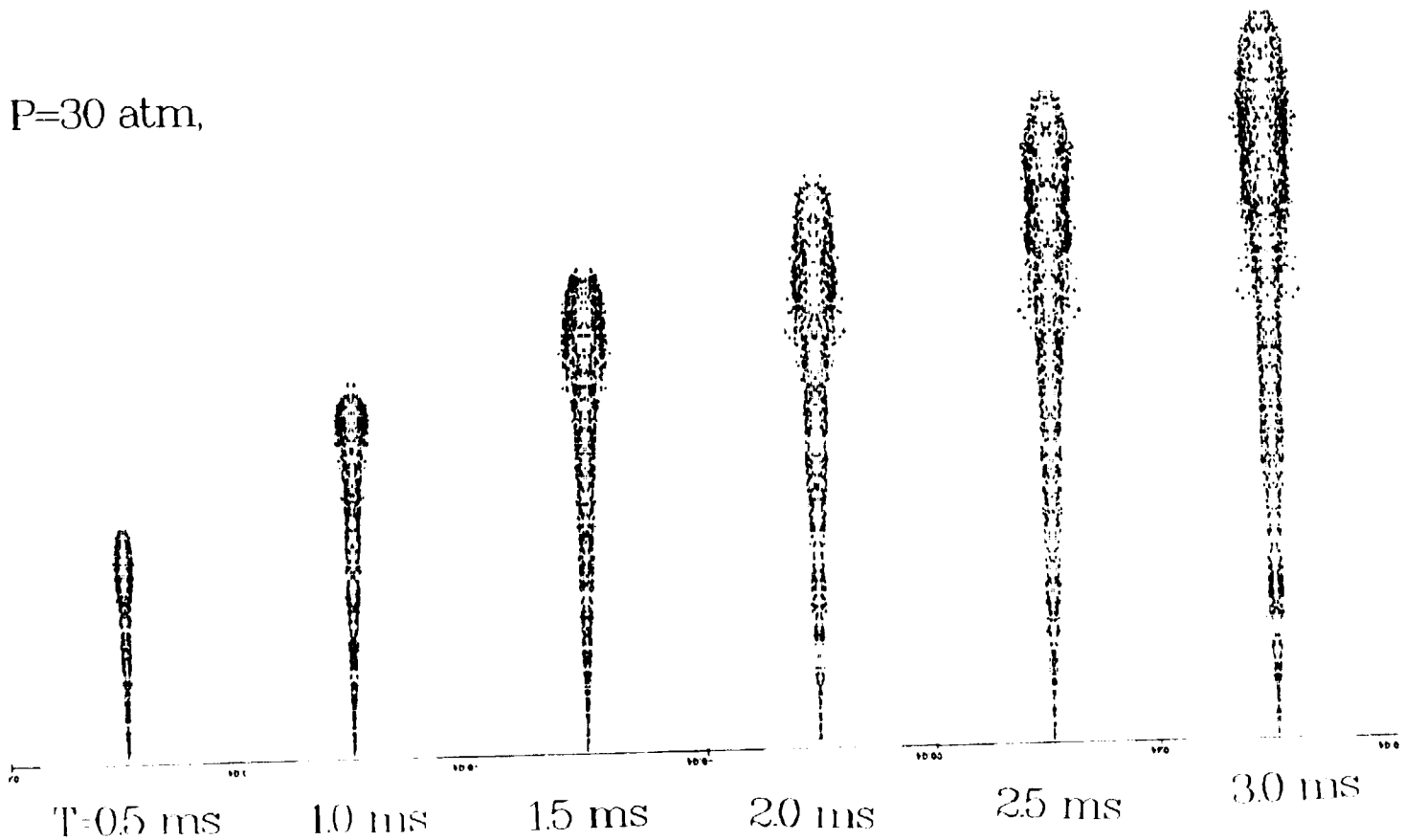

Figure 2. Single orifice jet in 30 Atm Chamber

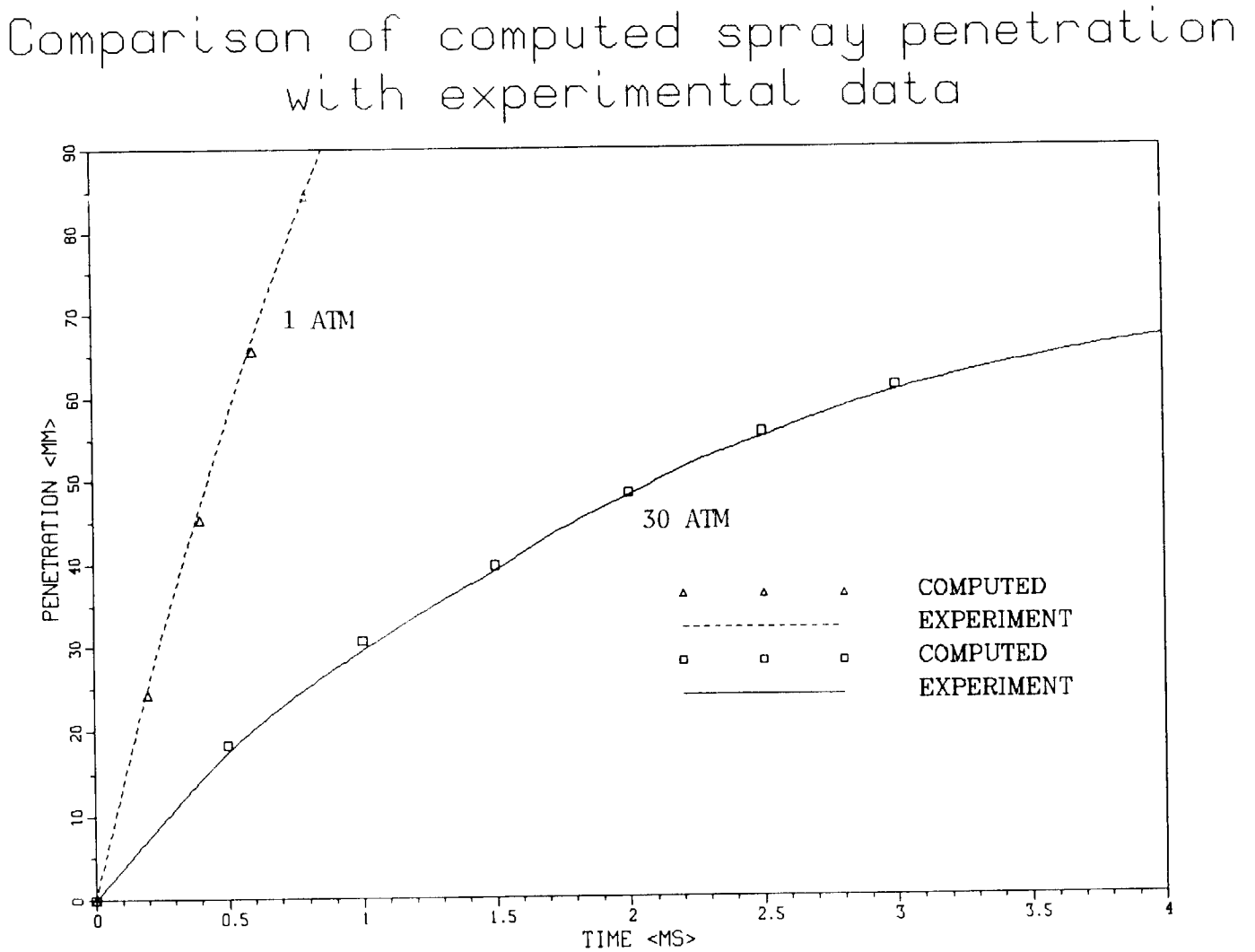

FIGURE 3.

TABLE 1

SINGLE-ORIFICE INJECTION PARAMETERS(Horiyasu)

Chamber Gas Pressure (ATM)	Injection Velocity (m/sec)	Gas Density (kg/m^3)	Mass Flow (kg/sec)	Sauter Mean Radius(SMR) μm	Eddy Viscosity (m^2/sec)
1	122.2	1.123	0.00726	5.0	7.1×10^{-4}
30	102.5	33.70	0.00609	5.0	5.0×10^{-4}

Fuel: Diesel fuel oil, $\rho_s = 840\ kg/m^3$

Ambient Gas: Nitrogen

Nozzle Diameter: 0.3 mm

TABLE 3

EFFICIENCY ASSESSMENT (CPU Time)

	MAST-2D		TEACH/PSIC	
SINGLE-ORIFICE SPAR	Particle #		Particle #	
41 × 61 Grid	600	126.9 sec	800	1420 sec
300 Time Steps	1200	135.7 sec		
HOLLOW CONE SPRAY	400	74.9 sec		
31 × 31 Grids			800	934 sec
200 Time Steps	1000	88.3 sec		

APPENDIX A

Numerical Predictions of Turbulent Recirculating Flows Using an Arbitrary-Lagrangian-Eulerian Scheme

by

CHUNG-MEE LEE

A THESIS

Submitted in partial fulfillment of the requirements
for the degree of Master of Science in Engineering
in
The Department of Mechanical Engineering
of
The School of Graduate Studies
of
The University of Alabama in Huntsville

1990

ACKNOWLEDGEMENTS

The author would like to sincerely thank to his advisor Dr. C. P. Chen for his patient guidance and support during the development of this thesis. The author also owes special acknowledgement and gratitude to Dr. Chen for his helpful insight, continual encouragement, and personal interest regarding this student's progress and understanding of the research material. He also expresses his appreciation to Dr. S. T. Wu and Dr. K. S. Hwang for serving as a committee member and for providing useful comments.

The author gratefully acknowledges the NASA-MSFC (NAG8-092), and the Department of Mechanical Engineering for financial support.

Finally, the author gives gratefulness to Pai-Lei Chen for her emotional and spiritual support during his graduate work.

ABSTRACT

The purpose of this study is to validate and further develop an existing Computational Fluid Dynamics code for simulating complex turbulent flows inside a liquid rocket combustion chamber. The ARICC (Advanced Rocket Injector/Combustor Code) Code is simplified and validated against benchmark flow situations for laminar and turbulent flows. The numerical method used in ARICC Code is re-examined for incompressible flow calculations. For turbulent flows, both the subgrid and the two equation $k - \epsilon$ turbulence models are studied. Cases tested include idealized Burger's equation in complex geometries and boundaries, a laminar pipe flow, a high Reynolds number turbulent flow, and a confined coaxial jet with recirculations. The accuracy of the algorithm is examined by comparing the numerical results with the analytical solutions as well as experimented data with different grid sizes.

TABLE OF CONTENTS

List of Tables

List of Figures

List of Symbols

A	area for regular cell
$\mathcal{A}$	area for momentum cell
c	adiabatic sound speed
c_v	specific heat at constant volume
c_μ c_D	constant values for $k-\epsilon$ model equation
$c_{1\epsilon}$ $c_{2\epsilon}$	constant values for $k-\epsilon$ model equation
F_α	the value of F at the center of cell face α
I	internal energy
K	thermal conductivity
k	turbulent kinetic energy
K_D	dimensionless constant in subgrid model
M	mass of regular cell
$\mathcal{M}$	mass of momentum cell
n_α	outward unit normal to the cell face
p	pressure
P_r	Prandtl number based on c_v
R	universal constant
Re	Reynolds number
T	temperature
U_b	bulk velocity
u	x direction's velocity
u_*	shear speed

v y direction's velocity

V volume for regular cell

$\mathcal{V}$ volume for momentum cell

w swirl velocity

x x direction (radial coordinate)

y y direction (axial coordinate)

α_0 β_0 constant for donor cell

β_{ij} relaxation coefficient

Δt time step

ϵ turbulence energy disspation rate

θ angle of swirl velocity

κ von Karman constant

Λ representative grid interval

μ viscosity of fluid

μ_L viscosity of laminar flow

μ_t eddy viscosity of turbulent flow

ν kinematic viscosity ($= \mu/\rho$)

ρ density

σ_k σ_ϵ constant values for $k - \epsilon$ model equation

τ_w wall shear stress

Superscripts

A value in phase A

B value in phase B

C value in phase C

c center values

m momentum cell values

n time step number

0	initial values for iteration
ν	iteration time step number

Subscripts

ij	vertice number or cell number
R	right side
T	top face
L	left side
B	bottom face
0	cell center values
α	cell face

CHAPTER I INTRODUCTION

Combustion flows involving liquid propellants inside a liquid rocket engine represent one the most complicated engineering flow systems in operation. The complexity stems from the existence of multiple zones with very different time and length scales within the same physical domain (Figure 1.1). The zones are in close proximity to each other and the processes are usually strongly coupled. In the injection zone, for instance, the major physical characteristics include those of multiphase flows, recirculation, high shear stresses, and steep pressure gradient. The multiphase flows involved are : a multispecies gaseous phase, incompressible liquid phase, and a particulate droplet phase. The dominant processes are liquid jet breakup and atomization, droplet-gas interactions and fluid-wall interactions. A short distance away from the injector, the characteristics of the flow become those of steep concentration gradients around droplets, turbulent mixing and diffusion, and dilute gas-liquid suspension flow. The critical processes become those of droplet transport, evaporation, and droplet heatup. Further downstream, the fuel/oxidizer mixture begins to combust. The flow is now characterized by high heat fluxes, a relatively large number of gaseous species, and temperature extremes that necessitate the consideration of real gas properties. The key processes are kinetic and equilibrium chemical reactions and species diffusion. Finally, in the post-combustion or

expansion zone, the fluid properties range from a "frozen" composition to near "dynamic equilibrium". There is high velocity gradient near walls and at the nozzle. The dominant processes of interest are transonic/supersonic flows and boundary layer effects.

As shown in Figure 1.1, all zones are coupled with each other. The first three zones in a typical rocket engine preburner, for example, the Space Shuttle Main Engine (SSME), comprise a volume of only about 1-inch diameter by 2-inch length. While different dominant processes can be identified in different zones, they are intrinsically coupled to each other.

In 1985, a comprehensive model for the simulation of detailed three-phase combustion flows inside combustion chamber was developed by Rocketdyne. The Rocketdyne Code (ARICC) is developed from CONCHAS-SPRAY of LANL (Los Alamos National Laboratory). The original CONCHAS-SPRAY code solves the equations of transient multicomponent chemically reactive fluid dynamics, together with those for the dynamics of an evaporating liquid spray. With few exception, reactive flow problems of practical interest are far too complex to be solved analytically. Quantitative theoretical analyses therefore require the use of numerical methods. CONCHAS-SPRAY is a time-marching code that solves finite difference approximations to the governing differential equations. The transient solution is marched out in a sequence of finite time increments called cycles or time steps. Values of the dependent variables on each cycle are calculated from those on the previous cycle. CONCHAS-SPRAY is a two-dimensional code, which assumes that the dependent variables depend on only two of the three spatial coordinates

because of symmetry. The effects of turbulence are represented by a simple subgrid scale (SGS) turbulence model, whose use is optional. The option is also provided to calculate boundary layer drag and heat transfer from a modified turbulent law of the wall. CONCHAS-SPRAY utilizes a partially implicit numerical scheme that is a variant of the ICE method (Harlow and Amsden, 1968, 1971). Spatial differences are formed with respect to a generalized finite-difference mesh or grid, which subdivide the region of interest into a number of small quadrilateral cells, or zones. The corners of the cells are called the vertices. The position of the vertices may be arbitrarily specified as function of time, thereby allowing a Lagrangian, Eulerian, or mixed description. Since the locations of the vertices are arbitrary, the cells are arbitrary quadrilaterals. This type of mesh is called an ALE (arbitrary Lagrangian-Eulerian) mesh (Hirt, Amsden and Cook, 1974; Pracht 1975), and is particularly useful for representing curved and/or moving boundary surfaces. Evaporating liquid sprays are represented by a discrete- particle technique (Dukowicz 1980), in which each computational particle represents a number of similar physical particles.

Simulation of gas phase and particle phase was completed in CONCHAS-SPRAY. In ARICC code, the volume of fluid method was added to account for dense spray (Figure 1.2). While the liquid phase is assumed to be incompressible with a constant density and temperature. The "pseudo-incompressible" treatment was used in ARICC, the inclusion of limited compressibility made the liquid iteration process much more stable and allowed much faster convergence (Liang et al. 1985).

The ARICC code is designed to simulate two-phase multi-species reacting flow

with spray droplets in either a two-dimensional or an axisymmetric with swirl configuration. The code is real-time accurate. It accounts for all the important physical processes involved in commonly encountered combustion devices either vigorously or using empirical models. Radiation, which is not significant in the case of liquid rocket combustion chambers, is not modeled (ARICC User's Manual).

The Deardorff's subgrid model is an algebraic model in which the "mixing length" is prescribed by the local grid size. In the last two decades, the advances of turbulence modeling has reach the point where reasonable good predictions of at least the mean velocity fields can be made by some advanced models. The purpose of this study is incorporate the so-called two equation kinetic energy (k)- energy dissipation rate (ϵ) turbulence model into the ARICC code for better presentation of turbulence field simulation. The $k - \epsilon$ model accounts for the history effect, as well as diffusion, sources of the characteristic velocity and length thus is more capable of handling complex flows such as the ones encountered in typical liquid engines. In the following chapters, numerical aspects of ALE-ICE schemes will be described. Several benchmark testing cases for laminar as well as turbulent flows will be performed to validate the implementations and performances of the turbulence models and the ALE-ICE scheme. Finally, conclusion and recommendations will be made.

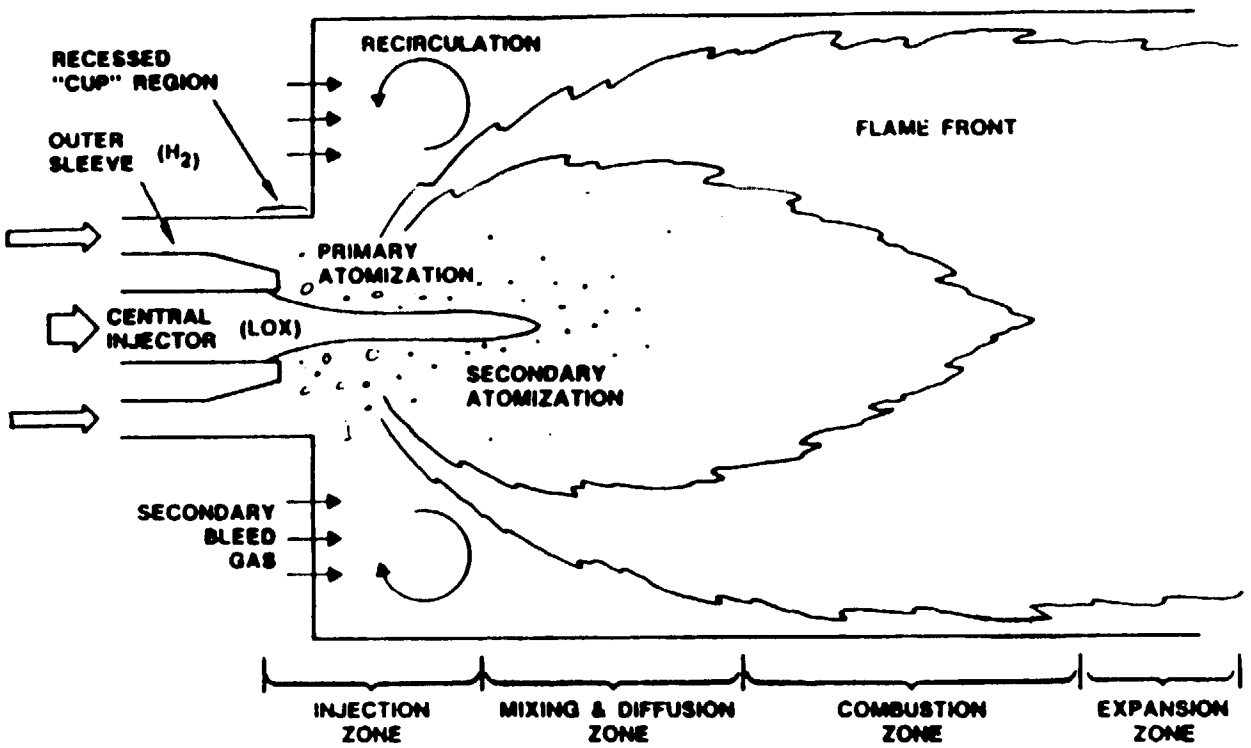

Figure 1. 1 Multi-zones in a Confined Coaxial Injector/Combustor

V O F (Volume of Fluid)

- ACTIVE CELLS DISTINGUISHED BY THEIR FLAG VALUES:

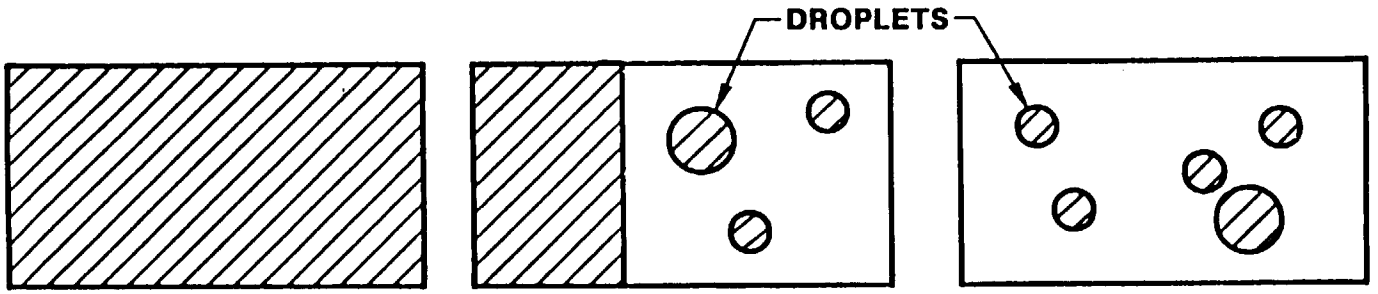

$$\text{DEF F} = \frac{\text{NET GASEOUS VOLUME (EXCL. DROPLETS)}}{\text{LIQUID VOL + NET GAS VOL.}}$$

- DROPLETS MAY EXIST IN CELLS WITH F > 0.0
- SINGLE-VALUED THERMODYNAMIC PROPERTIES FOR ALL CELLS
- PRESSURE IN FULLY LIQUID CELLS DETERMINED BY PRESSURE ITERATION SCHEME FOR IMCOMPRESSIBLE FLUID

Figure 1. 2 Volume of Fluid Algorithm

CHAPTER II MATHEMATICAL MODELS

A. Governing Equations

The governing equations in axisymmetric fluid flows are shown in cylindrical coordinate with x-y-θ coordinates and u-v-w velocities. The x direction is the axial coordinates and the y direction is the radial coordinates.

For conservation of mass, the governing equation is

$$\frac{\partial \rho}{\partial t} + \frac{1}{y}[\frac{\partial}{\partial x}(\rho y u) + \frac{\partial}{\partial y}(\rho y v)] = 0 \qquad (2.1.a)$$

For conservation of linear momentum of Newtonian fluid, the governing equations are given by

$$\frac{\partial}{\partial t}(\rho u) + \frac{1}{y}(\frac{\partial y\rho uu}{\partial x} + \frac{\partial y\rho uv}{\partial y}) = -\frac{\partial p}{\partial x} + \frac{1}{y}[\frac{\partial}{\partial x}(y\tau_{xx}) + \frac{\partial}{\partial y}(y\tau_{xy})] \qquad (2.2.a)$$

$$\frac{\partial}{\partial t}(\rho v) + \frac{1}{y}(\frac{\partial y\rho uv}{\partial x} + \frac{\partial y\rho vv}{\partial y}) = -\frac{\partial p}{\partial y} + \frac{1}{y}[\frac{\partial}{\partial x}(y\tau_{yx}) + \frac{\partial}{\partial y}(y\tau_{yy})] - \frac{\tau_{\theta\theta}}{y} + \frac{\rho w^2}{y} \qquad (2.2.b)$$

The angular momentum equation, which determines the swirl velocity w, is given by

$$\frac{\partial}{\partial t}(y\rho w) + \frac{1}{y}[\frac{\partial}{\partial x}(y^2\rho wu) + \frac{\partial}{\partial y}(y^2\rho wv)] = \frac{1}{y}[\frac{\partial}{\partial x}(y^2\tau_{x\theta}) + \frac{\partial}{\partial y}(y^2\tau_{y\theta})] \qquad (2.3)$$

For conservation of internal energy, the equation is given by

$$\frac{\partial}{\partial t}(\rho I) + \frac{1}{y}[\frac{\partial}{\partial x}(y\rho Iu) + \frac{\partial}{\partial y}(y\rho Iv)] = -\frac{p}{y}[\frac{\partial}{\partial x}(yu) + \frac{\partial}{\partial y}(yv)] +$$

$$\tau_{xx}(\frac{\partial u}{\partial x}) + 2\tau_{\theta\theta}(\frac{u}{y}) + \tau_{yy}(\frac{\partial v}{\partial y}) + 2y[\tau_{y\theta}\frac{\partial}{\partial y}(\frac{w}{y}) + \tau_{\theta x}\frac{\partial}{\partial x}(\frac{w}{y})] + \tau_{xy}(\frac{\partial u}{\partial x} + \frac{\partial v}{\partial y}) -$$
$$\frac{1}{y}[\frac{\partial}{\partial x}(yJ_x) + \frac{\partial}{\partial y}(yJ_y)] \tag{2.4}$$

where

$$\tau_{xx} = \mu[2\frac{\partial u}{\partial x} - \frac{2}{3}(\nabla \cdot \mathbf{u})]$$

$$\tau_{\theta\theta} = \mu[2\frac{u}{y} - \frac{2}{3}(\nabla \cdot \mathbf{u})]$$

$$\tau_{yy} = \mu[2\frac{\partial v}{\partial y} - \frac{2}{3}(\nabla \cdot \mathbf{u})]$$

$$\tau_{x\theta} = \tau_{\theta x} = \mu[y\frac{\partial}{\partial x}(\frac{w}{y})]$$

$$\tau_{\theta y} = \tau_{y\theta} = \mu[y\frac{\partial}{\partial y}(\frac{w}{y})]$$

$$\tau_{xy} = \tau_{yx} = \mu(\frac{\partial u}{\partial y} + \frac{\partial v}{\partial x})$$

and

$$\nabla \cdot \mathbf{u} = \frac{\partial u}{\partial x} + \frac{1}{y}\frac{\partial}{\partial y}(yv) = \frac{\partial u}{\partial x} + \frac{v}{y} + \frac{\partial v}{\partial y}$$

for the energy equation, the heat flux is

$$J_x = -K(\frac{\partial T}{\partial x})$$

$$J_y = -K(\frac{\partial T}{\partial y})$$

where ρ is the density, p is the pressure, u is the velocity in axial direction, v is the velocity in radial direction, T is the temperature, I is the internal energy of the fluid flow, μ is the viscosity of the fluid and K is the thermal conductivity.

For hot gases, equation of state is described by the ideal gas law

$$p = \rho RT \tag{2.5}$$

where R is the universal constant.

The preceding equations have been given in forms appropriate for laminar flows. In order to treat turbulent flows, the equations must be suitably averaged. Ensemble averages are used here. Whatever type of averaging process selected, instantaneous dependent variables are separated into mean and fluctuating components. The averaged equations are considerably simpler if the mean values are mass weighted (the so-called Favre averaging procedure) for compressible turbulent flows.

In order to show the turbulent motions and their interactions with the mean motion more explicitly, we follow a procedure due to Osborne Reynolds. Let us apply this procedure to the flow of a incompressible fluid with constant viscosity, constant density, isothermal flow. In this approach the instantaneous quantities are decomposed into mean and fluctuating parts, i.e.,

$$u_i = U_i + u_i'$$

$$p = P + p'$$

After insertion into equations (2.1) and (2.2) the following time averaged equations result

$$\rho(\frac{\partial U_i}{\partial t} + U_j\frac{\partial U_i}{\partial x_j}) = -\frac{\partial P}{\partial x_i} + \frac{\partial}{\partial x_j}[\mu_L(\frac{\partial U_i}{\partial x_j} + \frac{\partial U_j}{\partial x_i}) - \rho\overline{u_i'u_j'}] \tag{2.6}$$

For an incompressible fluid and constant viscosity, we come to the conclusion that the turbulence terms $\rho\overline{u_i'u_j'}$ can be interpreted as stresses on an element of the fluid in addition to the stresses determined by the pressure P and the viscous stresses. Because Reynolds was the first to give the equation for turbulent flow, the turbulent stresses $\rho\overline{u_i'u_j'}$ are often called Reynolds stresses.

In comparing the turbulence stresses in the equations of motion with the corresponding stresses caused by viscosity effects it is tempting to assume that the turbulence stresses act like the viscous stresses, that is, that they are directly proportional to the velocity gradient. Thus

$$\rho\overline{u_i'u_j'} = -\mu_t\left(\frac{\partial U_i}{\partial x_j} + \frac{\partial U_j}{\partial x_i}\right) \tag{2.7}$$

This assumption was made by Boussinesq, who introduced the concept of an "apparent," or "turbulence," or "eddy" viscosity μ_t. According to Boussinesq's concept, the eddy viscosity μ_t has a scalar value.

In this approximation the averaged flow equations become identical in form to the laminar ones; the transport coefficients (i.e., viscosity and thermal conductivity) are simply replaced by the appropriate turbulent transport coefficients which are much larger than the laminar values because of the additional transport caused by the turbulent fluctuations. Therefore, we use the equations summarized above even when the flow is turbulent, but with turbulent contributions added to the laminar values of the transport coefficients. The transport coefficients in ARICC are thus taken to be

$$\mu = \mu_L + \mu_t \tag{2.8}$$

$$K = \mu c_v / P_r \tag{2.9}$$

In this study, the dependence of μ_L on temperature is modeled by a curve fit, μ_L is laminar viscosity, P_r is the Prandtl number based on c_v, c_v is specific heat at constant volume, μ_t is a turbulent viscosity.

The eddy viscosity μ_t thus defined becomes a property of the flow encountered and requires modeling. The hierarchy of turbulence modeling has been reviewed extensively in the literature (see Deardorff (1971) and Jones and Lauder (1972)). In this study, the original zero equation subgrid turbulence model originally used in the CONCHAS-SPRAY and ARICC code will be validated against incompressible flows. In addition, a two- equation turbulence model ($k - \epsilon$ model) will be incorporated into the ARICC code. Brief descriptions of these two models are given below.

B. The Subgrid Turbulence Model

The subgrid model was suggested by Deardorff (1971). The local Reynolds stresses which arise from the averaging process were simulated by an eddy coefficient with magnitude limited in some way by the size of the averaging domain. When this domain is considered to be the grid volume of a detailed numerical integration, the eddy coefficient μ_t becomes a "subgrid scale" of "SGS" eddy coefficient. The formulation, which allows μ_t to be variable in space and time, is formulated as:

$$\mu_t = \frac{1}{\sqrt{2}} \rho K_D^2 \Lambda^2 (D_{11}^2 + D_{22}^2 + D_{33}^2 + 2D_{12}^2 + 2D_{13}^2 + 2D_{23}^2)^{\frac{1}{2}} \tag{2.10}$$

where

$$D_{11} = 2\frac{\partial u}{\partial x}, \quad D_{22} = 2\frac{\partial v}{\partial y}, \quad D_{33} = 2\frac{v}{y},$$

$$D_{12} = \frac{\partial u}{\partial y} + \frac{\partial v}{\partial x}, \quad D_{13} = y\frac{\partial}{\partial x}(\frac{w}{y}), \quad D_{23} = y\frac{\partial}{\partial y}(\frac{w}{y}) \tag{2.11}$$

where Λ is a representative grid interval and was taken to be the largest side length of the regular cell, D_{ij} is the magnitude of the local velocity deformation calculated on the finite-difference grid, and K_D is the dimensionless constant. Lilly (1967) has

estimated K_D with approximate knowledge of the Kolmogorov inertial-subrange constant α. He assumed that isotropic turbulence with such an inertial subrange was present in the problem being simulated numerically on scales both much greater and much less than the grid interval Λ. He also assumed $\Delta x = \Delta y = \Delta z = \Lambda$, and took the Reynolds averaging volume to be Λ^3. He found that

$$K_D \cong 0.23\alpha^{-\frac{3}{4}} \tag{2.12}$$

The essential techniques recommended by Williams (1969) were used independently by Deardorff (1970) in a steady of turbulent channel flow at large Reynolds number. K_D was suggested to be equal to 0.17.

C. The $k-\epsilon$ Turbulence Model

The field of turbulence modeling for single-phase flows is a rapidly expanding one and many proposals have been suggested. The chosen two-equation model is used to generate a turbulence length and velocity scale and these will be used to form a (non-constant) eddy viscosity. An appropriate velocity scale is $u' = k^{\frac{1}{2}}$. The $k-\epsilon$ model adopted here is the one developed by Jones and Launder (1972). In their paper, the equations was given by

$$\frac{\partial \rho k}{\partial t} + \frac{1}{y}[\frac{\partial}{\partial x}(y\rho uk) + \frac{\partial}{\partial y}(y\rho vk)] = \frac{1}{y}\{\frac{\partial}{\partial x}(\frac{\mu}{\sigma_k}y\frac{\partial k}{\partial x}) + \frac{\partial}{\partial y}(\frac{\mu}{\sigma_k}y\frac{\partial k}{\partial y})\} + G - c_D\rho\epsilon \tag{2.13}$$

$$\frac{\partial \rho\epsilon}{\partial t} + \frac{1}{y}[\frac{\partial}{\partial x}(y\rho u\epsilon) + \frac{\partial}{\partial y}(y\rho v\epsilon)] = \frac{1}{y}\{\frac{\partial}{\partial x}(\frac{\mu}{\sigma_\epsilon}y\frac{\partial \epsilon}{\partial x}) + \frac{\partial}{\partial y}(\frac{\mu}{\sigma_\epsilon}y\frac{\partial \epsilon}{\partial y})\} + \frac{(c_{1\epsilon}\epsilon G - c_{2\epsilon}\rho\epsilon^2)}{k} \tag{2.14}$$

where

$$G = \mu\{2[(\frac{\partial u}{\partial x})^2 + (\frac{\partial v}{\partial y})^2 + (\frac{v}{y})^2] + (\frac{\partial u}{\partial x} + \frac{\partial v}{\partial y})^2 + [y\frac{\partial}{\partial x}(\frac{w}{y})]^2 + [y\frac{\partial}{\partial y}(\frac{w}{y})]^2\}$$

μ_t is then expressed in terms of the turbulent kinetic energy k and the turbulent energy dissipation rate ϵ via the relation

$$\mu_t = c_\mu \rho k^2 / \epsilon \tag{2.15}$$

Philosophically, the strongest motivation for turning to more complex models is the observation that the algebraic model evaluates the turbulent viscosity only in terms of local flow parameters, yet a turbulence model ought to provide a mechanism by which upstream effects can influence the turbulence structure (and viscosity) downstream. Further, with the simplest models, ad hoc additions and corrections are frequently required to handle specific effects, and constants need to be changed to handle different classes of shear flows. To many investigators, it is appealing to develop a model general enough that specific modifications to the constants are not require to treat different classes of flows.

Note that the equations (2.13 $\sim$ 2.15) used above are valid only for high Reynolds number turbulent flows. In order to simulate low Reynolds number turbulent or transition flows including the near wall flows, the high Reynolds number $k - \epsilon$ model must be modified to incorporate viscous and low Reynolds number effect. In this thesis, only high Reynolds number $k - \epsilon$ model is considered. For this reason, the wall boundary conditions have to be constructed to avoid sublayer viscous effects and the wall function approach (to be described in Chapter 4) is adopted in this study.

In the equation (2.13) $\sim$ (2.15) the quantities σ_k, σ_ϵ, $c_{1\epsilon}$, $c_{2\epsilon}$, c_μ and c_D are model constants. Following Jones and Launder (1972) the values used are listing in Table 2.1.

Table 2.1 Constant values for $k-\epsilon$ model

σ_k	σ_ϵ	$c_{1\epsilon}$	$c_{2\epsilon}$	c_μ	c_D
1.00	1.30	1.44	1.92	0.09	1.00

Numerous other two-equation models have been suggested, Rubesin (1977) shows several comparisons between these models for incompressible flow, and overall they perform quite well, it is difficult to identify the best from the comparisons he has shown.

The $k-\epsilon$ turbulence model has enjoyed wide use because of its ability to predict the mean velocity field and spreading rate of many turbulent shear flows. A recent review of the applications of this model to a wide range of problems is given in Rodi (1982). Application of the $k-\epsilon$ model to heat and mass transfer problems is given in Shih (1982).

Despite the enthusiasm which is noted from time to time over two-equation models, it is perhaps appropriate to point out again the two major restrictions on this type of model. First, two-equation models of the type Boussinesq approximation holds. In algebraic models, μ_t is a local function whereas in two-equation models μ_t is a more general and complex function governed by two additional PDE's.

If the Boussinesq approximation fails, then two-equation models would fail. Obviously, in many flows the Boussinesq approximation models reality closely enough for engineering purposes.

The second shortcoming of two-equation models is the need to make assumptions in evaluating the various terms in the model transport equations, especially in evaluating the third-order turbulent correlations. This same shortcoming, however, plagues all higher-order closure attempts. These model equations contain no magic, they only reflect the best understanding and intuition of the originators. We can be optimistic, however, that the models can be improved by improved modeling of these terms.

CHAPTER III NUMERICAL METHODS – THE ALE-ICE SCHEME

The numerical method used in the ARICC code is the ALE-ICE (Arbitrary Lagrangian-Eulerian Mesh, Implicit Continuous-fluid Eulerian Technique) scheme which utilizes the fractional time step concept and solves the governing flow equations in unsteady forms. The temporal domain was discretized into time steps $\triangle t = t^{n+1} - t^n$ (n=0,1,2,...).

From t^n to t^{n+1} was called a cycle. There are two phases to be performed in one cycle. From t^n to the first intermediate step was called phase A. From phase A to next intermediate step was called phase B. Then from phase B, we go to next step phase C which is equivalent to t^{n+1} step. Phase A is an explicit Lagrangian calculation, phase B is an implicit pressure correction and phase C or n+1 step is a rezone calculation.

This separation of a calculational cycle into a Lagrangian phase and a convective flux, or rezone, phase originated in the Particle-in-Cell numerical method (Harlow 1955, Amsden 1966), and has since been used in many hydrodynamic computer codes. In the present technique the different phases can be combined in various ways to suit the requirements of individual problems. For example, in high speed problems, in which the Courant stability condition is not likely to be violated,

an explicit calculation is acceptable and the phase two iteration may be omitted, and for an explicit Lagrangian calculation only phase one is used.

The scheme uses arbitrary Lagrangian-Eulerian Mesh. This type mesh is made up of arbitrary quadrilateral. The equation was discretized by control volume or integral-balance approach, which preserves the local conservative properties of the differential equations. Spatial calculation domain is divided into a number of nonoverlapping control volumes such that there is one control volume surrounding each grid point. The differential equation is integrated over each control volume. The grid vertices may move in an arbitrarily prescribed manner. This capability includes the Lagrangian and Eulerian description as special cases.

A regular cell is shown in Figure 3.1. The index of the regular cell (ij) were regarded as horizontal and vertical coordinate. The indices (ij) also label the vertices, with the understanding that vertex (ij) is the (logical) lower left corner of cell (ij). The "center" (x^c_{ij}, y^c_{ij}) of the cell is defined by

$$x^c_{ij} = \frac{1}{4}(x_1 + x_2 + x_3 + x_4)$$

$$y^c_{ij} = \frac{1}{4}(y_1 + y_2 + y_3 + y_4) \tag{3.1}$$

In general, the point (x^c_{ij}, y^c_{ij}) is not the center of mass or volume of cell (ij).

The area of the cell in Figure 3.1 following CONCHAS-SPRAY (1982) and KIVA-II (1989) is calculated by the algebraic formula.

area = triangle 123 + triangle 134

$$4TR = \frac{1}{2}(y_1(x_2 - x_3) + y_2(x_3 - x_1) + y_3(x_1 - x_2))$$

$$ABL = \frac{1}{2}(y_1(x_3 - x_4) + y_3(x_4 - x_1) + y_4(x_1 - x_3))$$

$$A_{ij} \equiv ATR + ABL \tag{3.2}$$

The volumes corresponding to triangles 123 and 134 may be shown to be

$$VTR = \int_{\triangle(123)} ydxdy = \frac{1}{3}(y_1 + y_2 + y_3)ATR$$

$$VBL = \int_{\triangle(134)} ydxdy = \frac{1}{3}(y_1 + y_3 + y_4)ABL \tag{3.3}$$

The total cell volume is then given by

$$V_{ij} = \int_{A_{ij}} ydxdy = VTR + VBL \tag{3.4}$$

Momentum cell (ij) is centered about vertex (ij), as shown in Figure 3.2. A momentum cell has four of its corners at the centers of the four associated regular cells, the other four at the midpoints of the regular cell sides which meet at vertex (ij). Momentum cell's area and volume are $\mathcal{A}_{ij}^m$ and $\mathcal{V}_{ij}^m$. Those calculations are similar to the regular cell's calculation (equation 3.1 $\sim$ 3.4).

If the finite-difference representation for the equations has the conservative property, we must establish that the discretized version of the divergence theorem is satisfied. The differential equation is integrated over the area of a typical cell or momentum cell and use divergence theorem to transfer area integral to face integral.

$$\int\int_A \nabla \cdot \mathbf{F} dA = \int_s \mathbf{F} \cdot \mathbf{n} ds$$

We normally check this for a control volume consisting of the entire problem domain. To do this the integral on the left is evaluated by summing the difference

representation of the equation at all grid points. If the difference scheme has the conservative property, all terms will cancel except those which represent fluxes at the boundaries. It should be possible to rearrange the remaining terms to obtain identically a finite-difference representation of the integral on the right. The result will be a verification that the mass flux into the control volume equals the mass flux out. When the governing equation can be written in divergence form, we can be guided in this process by employing the Gauss divergence theorem to obtain the correct mathematical formulation for the physical law for a control volume. In practice, the control volume method has a history of leading quickly to expressions that prove to be more accurate than other possibilities near boundaries, probably because the method keeps the discrete nature of the solution method in view at all times. The distinctive characteristic of the control volume approach is that a "balance" of some physical quantity is made on the region in the neighborhood of a grid point. The discrete nature of the problem domain is always taken into account in the control volume approach which ensures that the physical law is satisfied over a finite region rather than only at a point as the mesh is shrunk to zero. It would appear that difference equations developed by the control volume approach would almost certainly have the conservative property.

Spatial differences are performed by integrating the differential term in question over the area of a typical cell (or momentum cell). If the term is of gradient or divergence form, its area integral is usually converted into a surface integral using the divergence theorem. The area integral of a time derivative is related to the derivative of the integral by means of the Reynolds transport theorem. The

area and surface integrals are performed under the assumption that the dependent variables with control volume approach are assumed uniform in each cell and/or on each face. Velocities are set at vertex and are regarded as uniform in momentum cell. All quantities are regarded as uniform with the value at the center of the cell face. Then, the line integrals over cell face are approximated by sums over the cell faces as shown in Figure 3.2.

$$\int_s \mathbf{F} \cdot \mathbf{n} ds \cong \sum_\alpha \mathbf{F}_\alpha \cdot \mathbf{n}_\alpha \triangle s_\alpha \tag{3.5}$$

where $\mathbf{F}_\alpha$ is the value of $\mathbf{F}$ at the center of cell face α, $\mathbf{n}_\alpha$ is the outward unit normal to the cell face, $\triangle s_\alpha$ is its length, and the faces are numbered in a counterclockwise order.

$$\mathbf{n}_\alpha \triangle s_\alpha = \mathbf{l}_\alpha \times \mathbf{k} = l_{\alpha y}\mathbf{i} - l_{\alpha x}\mathbf{j} \tag{3.6}$$

where $\mathbf{l}_\alpha$ is the vector of length $\triangle s_\alpha$ along cell face α in the counterclockwise direction, $\mathbf{k}$ is the unit vector out of the plane, $l_{\alpha x}, l_{\alpha y}$ are the x, y components of $\mathbf{l}_\alpha$ (Figure 3.3).

The velocities are located at vertex, then

$$u_{ij} = u(x_{ij}, y_{ij})$$

$$v_{ij} = v(x_{ij}, y_{ij}) \tag{3.7}$$

where u, v are the x, y components of fluid velocities. Thermodynamics variables and other scalar variables such as turbulence kinetic energy and energy dissipation rate are located at cell centers.

$$Q_{ij} = Q(x^c_{ij}, y^c_{ij}) \tag{3.8}$$

where $Q = p, \rho, T, I, k, \epsilon$.

A. Phase A : The Explicit Lagrangian Calculation

The explicit Lagrangian calculation was used in phase A. In this step velocities are advanced explicitly in time using pressure gradients and body forces computed from the currently available pressure and mesh coordinates. If viscous, elastic or other stresses are desired, they may be included at this stage as well. The total energy of each cell is also advanced in time to account for the work done by the body forces and other stresses, except those of pressure. Pressure work terms are included only after the implicit pressure calculation in phase B. This delay permits time-advanced pressures to be used in computing the work and ensures consistency with the velocities coming out of phase B. The vertices were assumed to move locally with the velocities. From this assumption, the convection terms of transport equations vanished. From continuity equation, we have

$$M_{ij}^A = M_{ij}^n = \int_{A_{ij}} y\rho dA = \rho_{ij}^n V_{ij}^n \tag{3.9}$$

From the Lagrangian assumption, the vertex position can be calculated by

$$x_{ij}^A = x_{ij}^n + u_{ij}^n \ \Delta t$$

$$y_{ij}^A = y_{ij}^n + v_{ij}^n \ \Delta t \tag{3.10}$$

and the volume V_{ij}^A can be calculated by the equations (3.1) $\sim$ (3.4) with all x^n's and y^n's replaced by x^A's and y^A's. The ρ_{ij}^A, p_{ij}^A were calculated by

$$\rho_{ij}^A = M_{ij}^A / V_{ij}^A \tag{3.11}$$

$$p_{ij}^{A} = \rho_{ij}^{A}\ R\ T_{ij}^{A} \tag{3.12}$$

The momentum equation was discretized by integrating over the momentum cell area $\mathcal{A}_{ij}^{m}$. In momentum cell $\mathcal{A}_{ij}^{m}$, the velocity is regarded as uniform, but the density was calculated by the associated four regular cell's density.

Therefore,

$$\int_{\mathcal{A}_{ij}^{m}} y\rho u_{ij} d\mathcal{A} = u_{ij} \int_{\mathcal{A}_{ij}^{m}} y\rho d\mathcal{A} = \mathcal{M}_{ij} u_{ij}$$

$$\int_{\mathcal{A}_{ij}^{m}} y\rho v_{ij} d\mathcal{A} = v_{ij} \int_{\mathcal{A}_{ij}^{m}} y\rho d\mathcal{A} = \mathcal{M}_{ij} v_{ij} \tag{3.13}$$

where $\mathcal{M}_{ij}$ is the mass of momentum cell (ij). The momentum equation in phase A was discretized by

$$\frac{\mathcal{M}_{ij}^{A} u_{ij}^{A} - \mathcal{M}_{ij}^{n} u_{ij}^{n}}{\Delta t} = -y_{ij}^{n} \sum_{\alpha=1}^{4} p_{\alpha}^{n}\ l_{\alpha x}^{n} + \sum_{\alpha=1}^{8} (y\tau_{yy}\Delta x + y\tau_{yx}\Delta y - \tau_{\theta\theta}\mathcal{A}^{m})_{\alpha}^{n} + \mathcal{M}_{ij}^{n} \frac{{w_{ij}^{n}}^{2}}{y_{ij}^{A}}$$

$$\frac{\mathcal{M}_{ij}^{A} v_{ij}^{A} - \mathcal{M}_{ij}^{n} v_{ij}^{n}}{\Delta t} = -y_{ij}^{n} \sum_{\alpha=1}^{4} p_{\alpha}^{n}\ l_{\alpha y}^{n} + \sum_{\alpha=1}^{8} (y\tau_{xy}\Delta x + y\tau_{xx}\Delta y)_{\alpha}^{n} \tag{3.14}$$

where the p_{α}^{n} is the pressure of the regular cell in which face α lies, the summation are over the four faces which are orthogonal to the pressure directions. Δx and Δy are the distance of the cell center to the cell face in x direction or y direction.

The diffusion terms summation are over the eight faces of momentum cell (ij), it has been shown in Figure 3.2. For evaluating viscous stresses, the regular cell was partitioned into four quadrants by the momentum cell faces which meet at the cell center 0 (Figure 3.4). These faces are labeled R, T, B, L. Each vertices has two faces from one regular cell, and eight faces from four associated regular cells. Faces B, R are two of the eight faces of momentum cell centered at vertex 1, faces R, T

are two of the eight faces of the momentum cell centered at vertex 2 and so on. The velocities at point 0 are defined as the average velocities of the four vertices values.

$$u_0 = \frac{1}{4}(u_1 + u_2 + u_3 + u_4)$$

$$v_0 = \frac{1}{4}(v_1 + v_2 + v_3 + v_4) \tag{3.15}$$

The viscous stresses on faces R, T, L, B were described below. First, the partial derivatives of u, v with respect to x, y in faces R which shown in Figure 3.4 were calculated by the triangle rule.

$$[\frac{\partial u}{\partial x}]_R = \frac{y_{20}\ u_{10} - y_{10}\ u_{20}}{x_{10}\ y_{20} - x_{20}\ y_{10}}$$

$$[\frac{\partial v}{\partial y}]_R = \frac{x_{10}\ v_{20} - x_{20}\ v_{10}}{x_{10}\ y_{20} - x_{20}\ y_{10}} \tag{3.16}$$

where

$$u_{ab} = u_a - u_b, v_{ab} = v_a - v_b$$

$$x_{ab} = x_a - x_b, y_{ab} = y_a - y_b$$

$$a, b = 0, 1, 2, 3, 4$$

and the others faces T, L, B are obtained by the permutations (R, 1, 2) → (T, 3, 4) → (B, 4, 1). The diffusion term is evaluated as the sum of four contributions, one from each of the regular cell shown in Figure 3.4 contributes to each of the vertices 1, 2, 3, 4.

B. Phase B : Pressure Correction

In phase B, the vertex positions are determined by the equations

$$x_{ij}^B = x_{ij}^n + u_{ij}^B\ \triangle t$$

$$y_{ij}^B = y_{ij}^n + v_{ij}^B \ \Delta t \tag{3.17}$$

From those vertex positions x_{ij}^B, y_{ij}^B, the cell volume V_{ij}^B in phase B can be calculated by the equation (3.1) $\sim$ (3.4). The cell mass is not changed in this step, because the continuity equation.

$$M_{ij}^B = M_{ij}^A \tag{3.18}$$

Then the density in this step is decided by

$$\rho_{ij}^B = M_{ij}^B / V_{ij}^B = M_{ij}^A / V_{ij}^B = \rho_{ij}^A V_{ij}^A / V_{ij}^B \tag{3.19}$$

Therefore, the pressure can be calculated by

$$p_{ij}^B = \rho_{ij}^B \ R \ T_{ij}^B \tag{3.20}$$

For isothermal process, we have $T_{ij}^B = T_{ij}^A = T_{ij}^n$.

In phase B, the momentum equations was reduced to

$$\mathcal{M}_{ij}^A \frac{u_{ij}^B - u_{ij}^A}{\Delta t} = -y_{ij}^n \sum_{\alpha=1}^{4} (p_\alpha^B - p_\alpha^A) l_{\alpha y}^n$$

$$\mathcal{M}_{ij}^A \frac{v_{ij}^B - v_{ij}^A}{\Delta t} = -y_{ij}^n \sum_{\alpha=1}^{4} (p_\alpha^B - p_\alpha^A) l_{\alpha x}^n \tag{3.21}$$

In equation (3.21) the summations are over faces of momentum cell (ij), p_α is the pressure of the regular cell in which face α lies.

The methodology described above is valid for compressible flows since equation of state is utilized. As for the unsteady Navier-Stokes equations, the numerical difficulty lies in the constraint $\nabla \cdot \mathbf{V} = 0$. In the steady case, this difficulty can

be surmounted by using the so-called Pseudocompressible method. The method has been introduced by Chorin (1967). The principle of the method is to consider the solution of the steady equations (2.1) as the limit when $t \to \infty$ of the solution of unsteady equations obtained by associating the unsteady momentum equation (2.2) with a perturbed divergence equation in order to get a system of equations of evolution which can be easily solved by standard methods.

The Chorin method is established by first writing a perturbed continuity equation

$$\frac{\partial p}{\partial t} + c^2 \rho \nabla \cdot \mathbf{V} = 0 \tag{3.22}$$

where c^2 is an arbitrary constant. This equation has no physical meaning before the steady state $\partial/\partial t = 0$ is reached. So the constraint $\nabla \cdot \mathbf{V} = 0$ is satisfied at convergence only. The method, which consists of solving equation (2.2) and (3.22) can be called a pseudo-unsteady method because the time t involved has no physical meaning. The parameter c^2 in equation (3.22) must be chosen to ensure convergence, i.e., to ensure the existence of a steady numerical solution of the system.

The term "pseudocompressible method" (Chorin 1967) can be derived from the Navier-Stokes equations for a compressible fluid whose state law would be

$$p = c^2 \rho$$

with c^2 = constant. However, possible numerical difficulties can be associated with the use of a very large value of c^2, and hence the pseudocompressible method will likely have the most value in the computation of steady solutions. In this way, it can be considered a procedure to build a special iterative method for solving the

steady problem. For incompressible flows, the momentum equations must coupled with the continuity equation. Continuity equation was discretized by

$$(p^B - p^n) + \rho c^2 (\frac{V^B}{V^n} - 1) = 0 \tag{3.23}$$

The equations (3.17) $\sim$ (3.21) for compressible flow or (3.17), (3.21), (3.23) for incompressible flow are an implicit system of equations for unknown quantities x_{ij}^B, y_{ij}^B, u_{ij}^B, v_{ij}^B and p_{ij}^B. One of the major problems in machine computations is to find an effective method of solving a system of n simultaneous linear equations, particularly if n is large. There is, of course, no best method for all problem because the goodness of a method depends to some extent upon the particular system to be solved.

This implicit system can be solved by a Successive Over Relaxation (SOR) scheme. We now proceed to describe the SOR. Let the iteration index be ν, which will be displayed as a superscript in parentheses. SOR is specified by giving the prescription for advancing all quantities from iteration ν to iteration $\nu + 1$. The vertex positions are advanced first:

$$x_{ij}^{(\nu+1)} = x_{ij}^n + u_{ij}^{(\nu)} \, \Delta t$$

$$y_{ij}^{(\nu+1)} = y_{ij}^n + v_{ij}^{(\nu)} \, \Delta t \tag{3.24}$$

the quantities $(x_{ij}^{(\nu+1)}, y_{ij}^{(\nu+1)})$ then determine $V_{ij}^{(\nu+1)}$ in the usual way. The pressure change is computed by the relaxation formula for compressible flow

$$p_{ij}^{(\nu+1)} = p_{ij}^{(\nu)} - \beta_{ij} [p_{ij}^{(\nu)} - \frac{RT_{ij}^{(\nu)}}{V_{ij}^{(\nu+1)}} M_{ij}^A] \tag{3.25.a}$$

where

$$T_{ij}^{(\nu)} = T_{ij}^{A} - \frac{\phi_1 p_{ij}^{(\nu)}}{M_{ij}^{A}(c_v)_{ij}^{A}}(V_{ij}^{(\nu+1)} - V_{ij}^{n})$$

for incompressible flow, the equation changed to

$$p_{ij}^{\nu+1)} = p_{ij}^{(\nu)} - \beta_{ij}[(p_{ij}^{(\nu)} - p_{ij}^{n}) + \rho c^2(\frac{V_{ij}^{(\nu+1)}}{V_{ij}^{n}} - 1)] \qquad (3.25.b)$$

and β_{ij} is a relaxation coefficient defined below. Finally, the velocity is updated according to

$$\mathcal{M}_{ij}^{A} u_{ij}^{(\nu+1)} = \mathcal{M}_{ij}^{A} u_{ij}^{A} - \Delta t y_{ij}^{n} \sum_{\alpha} (p_{\alpha}^{(\nu+1)} - p_{\alpha}^{n}) l_{\alpha y}^{n}$$

$$\mathcal{M}_{ij}^{A} v_{ij}^{(\nu+1)} = cal M_{ij}^{A} v_{ij}^{A} - \Delta t y_{ij}^{n} \sum_{\alpha} (p_{\alpha}^{(\nu+1)} - p_{\alpha}^{n}) l_{\alpha x}^{n} \qquad (3.26)$$

Since equation (3.25) determines the pressure change

$$\delta p_{ij}^{(\nu)} \cong p_{ij}^{(\nu+1)} - p_{ij}^{(\nu)} \qquad (3.27)$$

It is convenient to rewrite equation (3.26) in terms of

$$\delta u_{ij}^{(\nu)} = u_{ij}^{(\nu+1)} - u_{ij}^{(\nu)}$$

$$\delta v_{ij}^{(\nu)} = v_{ij}^{(\nu+1)} - v_{ij}^{(\nu)} \qquad (3.28)$$

We then obtain

$$M_{ij}^{A} \delta u_{ij}^{(\nu)} = -\Delta t y_{ij}^{n} \sum_{\alpha} \delta p_{\alpha}^{(\nu)} l_{\alpha y}^{n}$$

$$M_{ij}^{A} \delta v_{ij}^{(\nu)} = -\Delta t y_{ij}^{n} \sum_{\alpha} \delta p_{\alpha}^{(\nu)} l_{\alpha x}^{n} \qquad (3.29)$$

Equation (3.29) is more convenient for numerical purposes than equation (3.26), as it allows one to avoid saving the u_{ij}^{A}, v_{ij}^{A}.

The iteration is initialized by setting

$$u_{ij}^{(0)} = u_{ij}^{A}, \quad v_{ij}^{(0)} = v_{ij}^{A}, \quad p_{ij}^{(0)} = p_{ij}^{n} + \overline{\Delta p} \tag{3.30}$$

where $\overline{\Delta p}$ is an estimated change in overall pressure level (defined below), and the final converged values are given by

$$(x_{ij}^{B}, y_{ij}^{B}, p_{ij}^{B}, u_{ij}^{B}, v_{ij}^{B}) = \lim_{\nu \to \infty} (x_{ij}^{(\nu)}, y_{ij}^{(\nu)}, p_{ij}^{\nu}, u_{ij}^{(\nu)}, v_{ij}^{(\nu)}) \tag{3.31}$$

of course, the limit $\nu \to \infty$ is achieved for all practical purposes at some finite value of ν; this value is determine by a convergence criterion and the iteration is terminated at that point. After the iteration has converged. V_{ij}^{B} is known and the densities ρ_{ij}^{B} are calculated by (3.17). All quantities are updated by its relative equations.

The relaxation coefficient β_{ij} for compressible flow is given by

$$\beta_{ij} = w[1 - RM_{ij}^{A} \frac{\partial}{\partial p_{ij}} (\frac{T_{ij}}{V_{ij}})]^{-1} \tag{3.32.a}$$

for incompressible flow is changed to

$$\beta_{ij} = w[\frac{\partial S_{ij}}{\partial p_{ij}}]^{-1} \tag{3.32.b}$$

where

$$S_{ij} = (p_{ij}^{(\nu)} - p_{ij}^{n}) + \rho c^2 (\frac{V_{ij}^{(\nu+1)}}{V_{ij}^{n}} - 1)$$

where V_{ij} and T_{ij} are here to be considered as function of p_{ij}; these functions are implicitly determines by equation (3.1), (3.2), (3.23), (3.24), (3.29). The derivative in equation (3.31) is evaluated numerically by inserting a small pressure perturbation into cell (i,j) and calculating the resulting change in (T_{ij}/V_{ij}) for compressible

flow or S_{ij} for incompressible flow. The coefficient w in equation (3.31) is the usual overrelaxation parameter, which may be varied in the range $0 < w < 2$ to accelerate convergence. Best results are usually obtained with $w > 1$.

C. Phase C or n+1 Step : Rezone Calculation

In phases A and B, the vertices were assumed to move with the fluid, based on the Lagrangian calculation. If the calculation in phase C used Lagrangian technique, the rezone procedure is not needed. If the Eulerian technique was used, the new mesh should be remapped into its old mesh. The vertex positions were determined by either of the two ways or by other prescribed methods. They were assumed to move with the fluid (Lagrangian mesh)

$$x_{ij}^{n+1} = x_{ij}^{B}$$

$$y_{ij}^{n+1} = y_{ij}^{B} \qquad (3.33.a)$$

or they were not move with the fluid (Eulerian mesh)

$$x_{ij}^{n+1} = x_{ij}^{B} - u_{ij}^{B}\triangle t$$

$$y_{ij}^{n+1} = y_{ij}^{B} - v_{ij}^{B}\triangle t \qquad (3.33.b)$$

In Lagrangian technique, phase C is not needed. So in phase C, only the Eulerian calculation is discussed. From equation (3.33), the volume V_{ij}^{n+1} of phase C was calculated by equations (3.1) $\sim$ (3.4), the mass was calculated by equation (3.23) from continuity equation.

$$M_{ij}^{n+1} = M_{ij}^{B} + \sum_{\alpha=1}^{8} [\rho]_{\alpha}^{B}\ \delta V_{\alpha} \qquad (3.34)$$

where the δV_α is done by geometrically calculating the volume swept out by each regular cell face as it moves from its Lagrangian position (determined by the x_{ij}^B, y_{ij}^B) to its final position (determined by the x_{ij}^{n+1}, y_{ij}^{n+1}), the quantities in $[\rho]$ are chosen from the δV_α located. The relationships are shown in Figure 3.5.

Let δV_α be the signed volume associated with the quadrilateral having swept by two opposing sides cell face α from phase B to phase n+1. This volume is evaluated by equations (3.1) $\sim$ (3.4) and the algebraic sign of δV_α can be decided.

The density in n+1 phase was decided by

$$\rho_{ij}^{n+1} = M_{ij}^{n+1} / V_{ij}^{n+1} \tag{3.35}$$

Similarly, the momentum equation was calculated by

$$\mathcal{M}_{ij}^{n+1} u_{ij}^{n+1} = \mathcal{M}_{ij}^{B} u_{ij}^{B} + \sum_{\alpha=1}^{8} [\rho u]_\alpha^B \ \delta \mathcal{V}_\alpha$$

$$\mathcal{M}_{ij}^{n+1} v_{ij}^{n+1} = \mathcal{M}_{ij}^{B} v_{ij}^{B} + \sum_{\alpha=1}^{8} [\rho v]_\alpha^B \ \delta \mathcal{V}_\alpha \tag{3.36}$$

where $\delta \mathcal{V}_\alpha$ is the momentum cell similar to the δV_α for the regular cells. The α's in δV_α is the α face of the regular cell, $\alpha = 1, 2, 3, 4$. The α's in $\delta \mathcal{V}_\alpha$ is the α face of the momentum cells, $\alpha = 1, 2, 3, 4, 5, 6, 7, 8$.

The cell quantities $[\rho]_\alpha^B$, $[\rho u]_\alpha^B$, $[\rho v]_\alpha^B$ were determined by the donor cell scheme. Let the interested regular cell α be called cell 1 and the neighboring cell which is connected to the cell face α be called cell 2. The cell quantities were evaluated as an upwind-weighted average of the quantity of cell face 1 and cell face 2. First, the upwind cell or donor cell should be decided by the sign of δV : if $\delta V > 0$, the cell 2

is the upwind or donor cell which cell 1 is the downwind or acceptor cell. and vice verse.

Therefore, those quantities was defined

$$Q_d^B = \begin{cases} Q_2^B & if \quad \delta V_\alpha > 0 \\ Q_1^B & if \quad \delta V_\alpha < 0 \end{cases}$$

$$Q_a^B = \begin{cases} Q_1^B & if \quad \delta V_\alpha > 0 \\ Q_2^B & if \quad \delta V_\alpha < 0 \end{cases} \tag{3.37}$$

where $Q = \rho, \rho u, \rho v$, d is referred to the donor cell quantity and a is the acceptor cell quantity. In $\rho]_\alpha^B$, $[\rho u]_\alpha^B$, $[\rho v]_\alpha^B$, a partial donor cell scheme was described.

$$Q_\alpha^B = \frac{1}{2} Q_d^B (1 + \alpha_0 + \beta_0 C) + \frac{1}{2} Q_a^B (1 - \alpha_0 - \beta_0 C) \tag{3.38}$$

where α_0 and β_0 are adjustable coefficients. $(0 \leq \alpha_0 + \beta_0 \leq 1)$ and

$$C = \frac{2|\delta V|}{V_1 + V_2} \tag{3.39}$$

where V_1, V_2 is the area of cell 1, cell 2.

In equation (3.38), when $\alpha_0 = 0$ and $\beta_0 = 0$, this scheme represents the centered differencing approximation for the convection term. which is unconditionally unstable. If $\alpha_0 = 1$ and $\beta_0 = 0$, this scheme is the donor cell or upwind differencing scheme. It is stable, but too diffusive for most calculations. If $\alpha_0 = 0$ and $\beta_0 = 1$, the scheme is an interpolated donor cell scheme. A weighted factor which is an average of the centered and the donor cell differencing is added. which makes this scheme more stable. This interpolation scheme is also less diffusive than the donor cell differencing by a factor C.

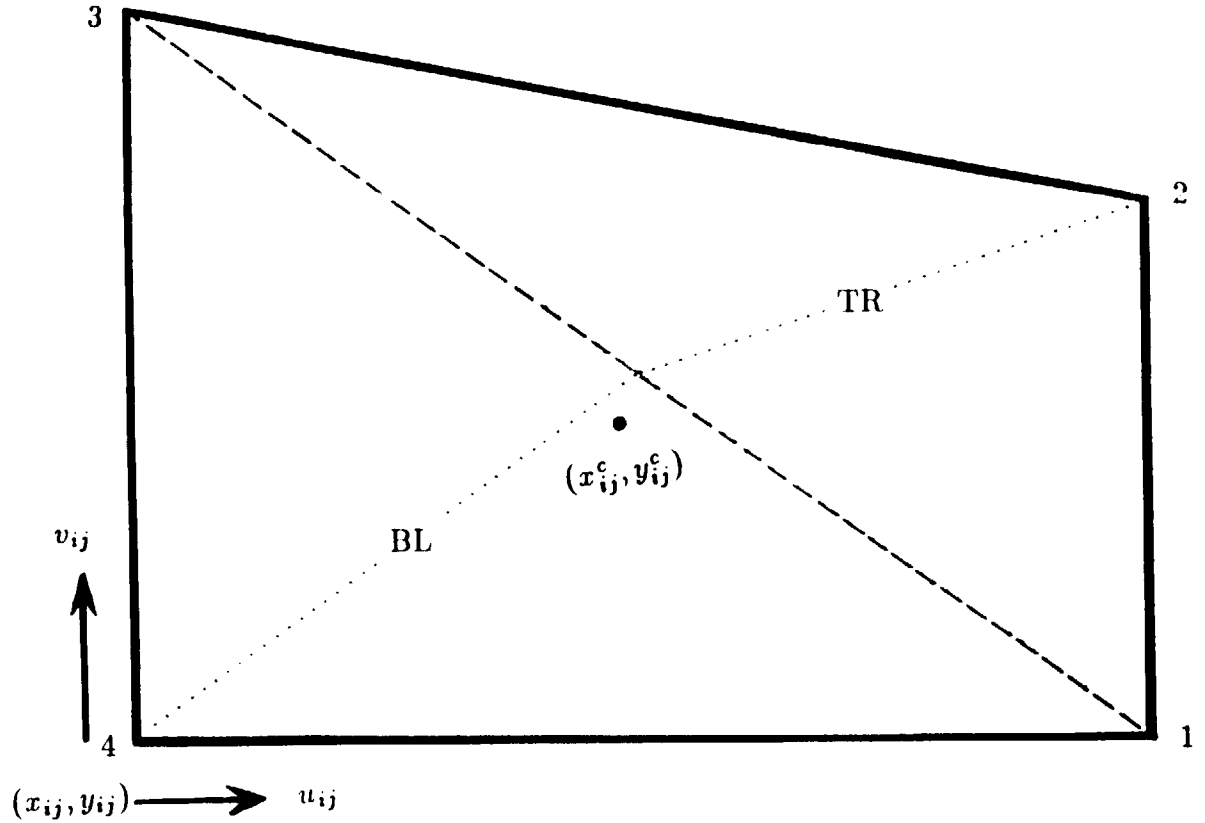

Figure 3. 1 Geometry of Regular Cell

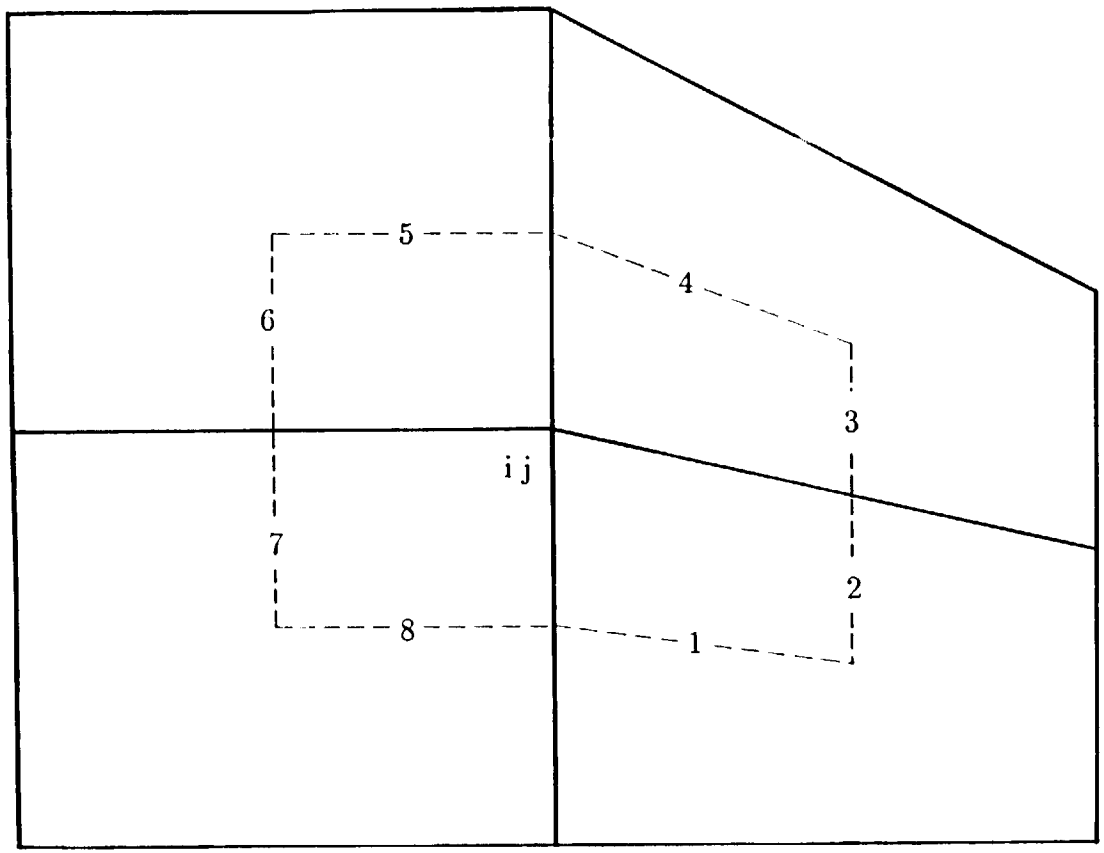

Figure 3. 2 Geometry of Momentum Cell

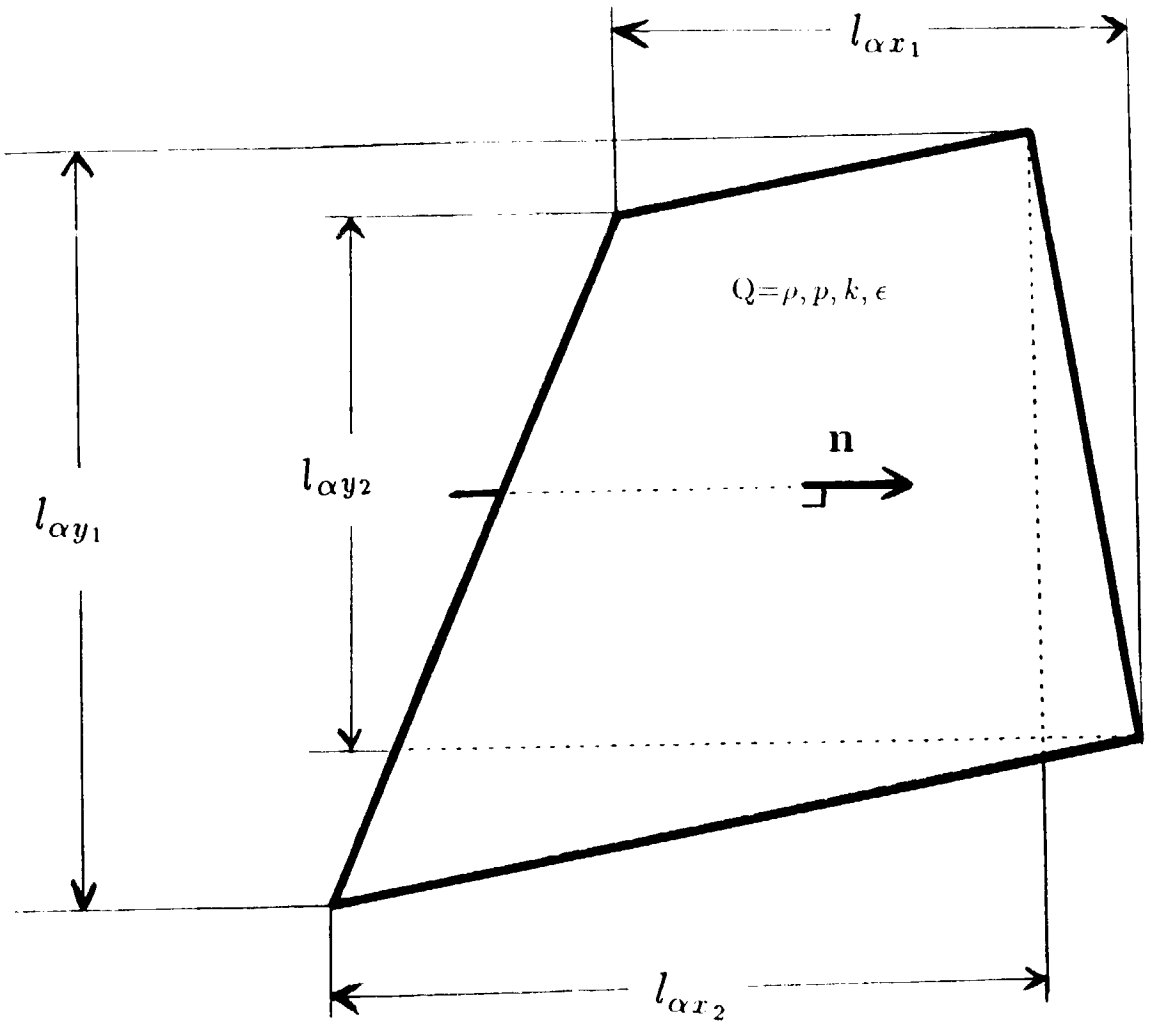

Figure 3. 3 The Gradient of Cell-centered Quantity Q on Cell Face α

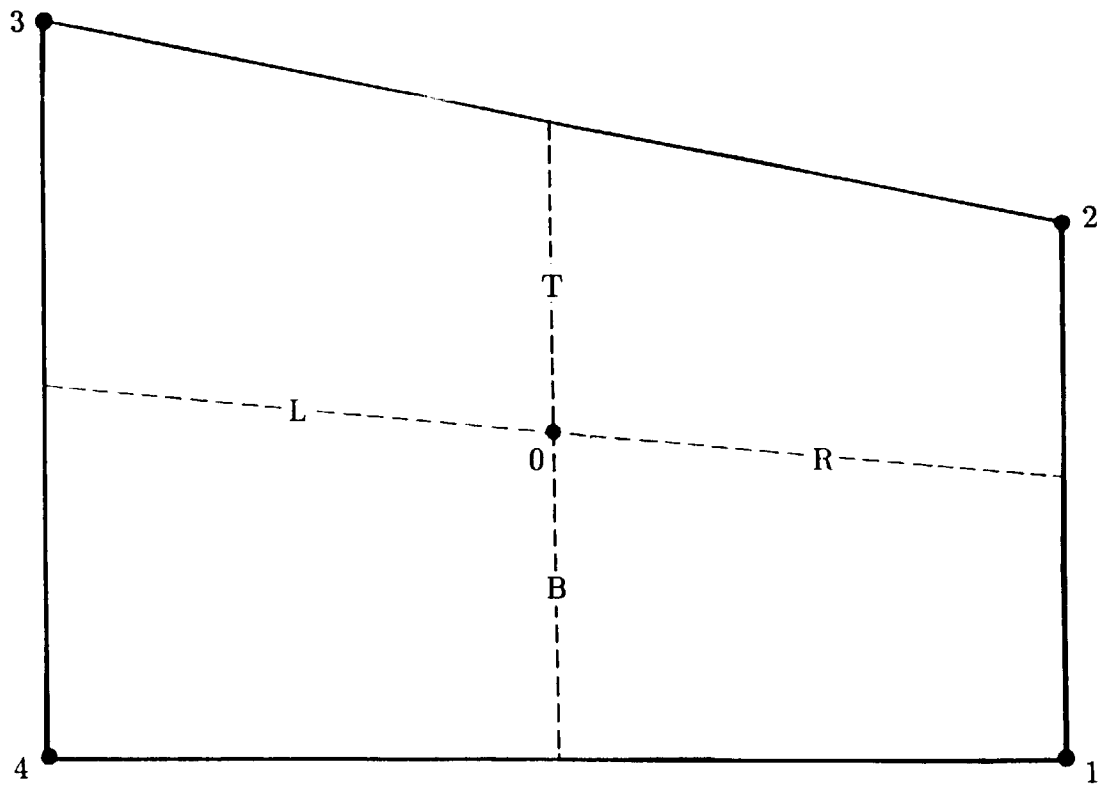

Figure 3. 4 Regular Cell used for Differencing Viscous Stress

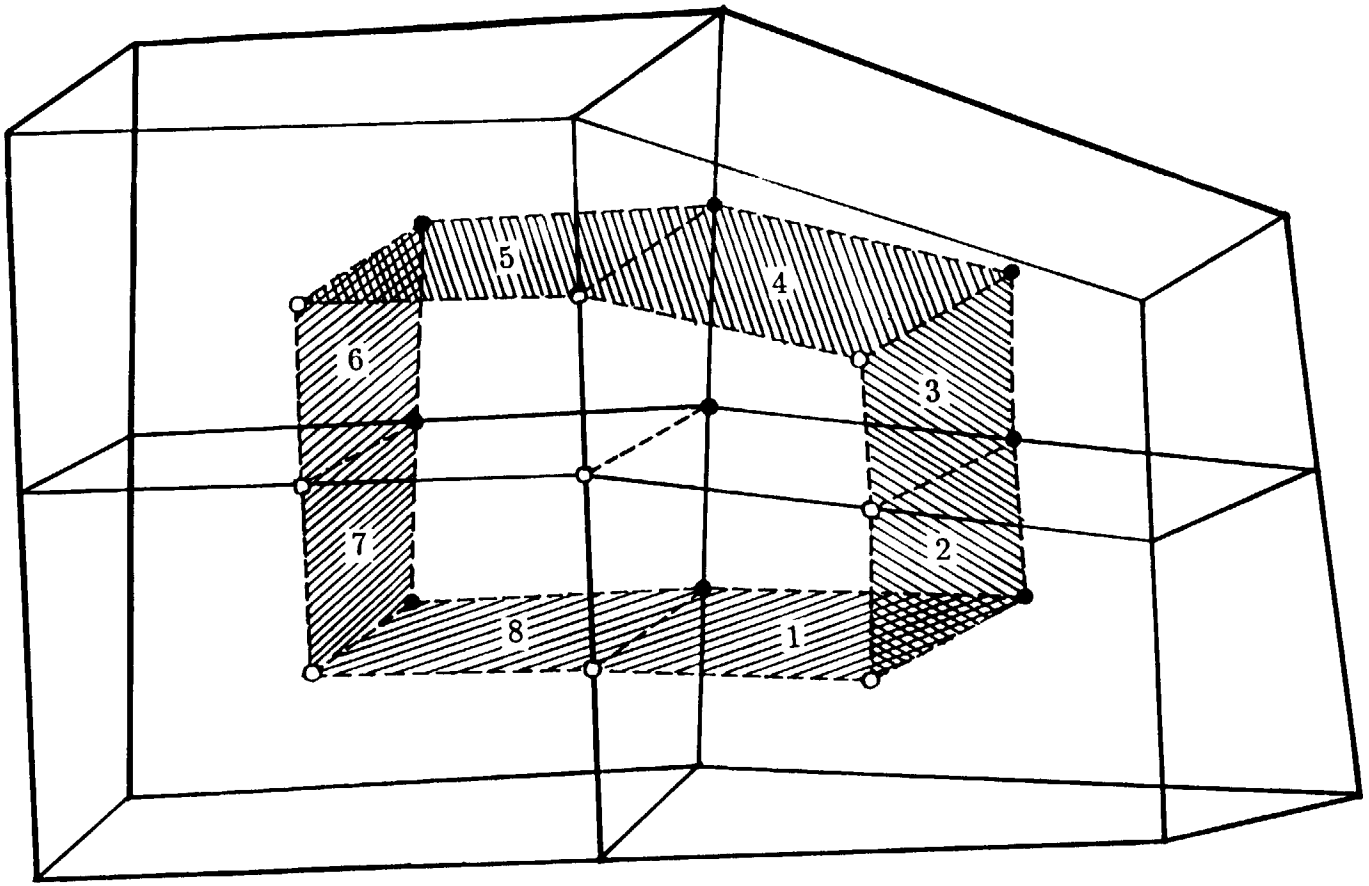

Figure 3. 5 Donor Cell used at Momentum Calculation

CHAPTER IV IMPLEMENTATION OF TURBULENCE MODELS IN THE ALE-ICE SCHEME

The implementations of the two turbulence models described in Chapter 2 as well as the appropriate boundary conditions will be described in this Chapter.

A. Subgrid Scale Eddy Viscosity

The eddy viscosity μ_t is a cell center variable and the velocity gradients in equation (2.8) are evaluated for each of the two triangles into which the cell is divided (Figure 3.1) using the triangle rule:

$$(\frac{\partial \phi}{\partial x})_{TR} = \frac{y_{23}\ \phi_{13} - y_{13}\ \phi_{23}}{x_{13}\ y_{23} - x_{23}\ y_{13}}$$

$$(\frac{\partial \phi}{\partial y})_{TR} = \frac{x_{13}\ \phi_{23} - x_{23}\ \phi_{13}}{x_{13}\ y_{23} - x_{23}\ y_{13}} \tag{4.1}$$

where $\phi = u, v,$ or w and

$$\phi_{ab} = \phi_a - \phi_b \ ,$$

$$x_{ab} = x_a - x_b \ ,$$

$$y_{ab} = y_a - y_b$$

and

$$a, b = 1, 2, 3, 4$$

The derivatives of $(\partial\phi/\partial x)_{BL}$ and $(\partial\phi/\partial y)_{BL}$ are obtained by the permutation (TR, 1, 2, 3) $\rightarrow$ (BL, 1, 3, 4). From those derivatives the quantities D_{ij}^2 of equation

(2.9) was computed by

$$D_{ij}^2 = \max[(D_{ij})_{TR}^2, (D_{ij})_{RI}^2] \tag{4.2}$$

Those results were substituted to equation (2.8), and the turbulent viscosity μ_t is obtained.

B. $k-\epsilon$ Turbulence Model

The $k-\epsilon$ model requires solving two extra transport equations. In phase A, the Lagrangian formulation excluding the convection terms was implemented

$$\frac{M^A k^A - M^n k^n}{\triangle t} = \sum_{\alpha=1}^{4} \{(y\frac{\mu}{\sigma_k})\frac{\partial k}{\partial x} + (y\frac{\mu}{\sigma_k})\frac{\partial k}{\partial y}\}_\alpha^n +$$

$$G^n - c_D \rho^n \epsilon^n$$

$$\frac{M^A \epsilon^A - M^n \epsilon^n}{\triangle t} = \sum_{\alpha=1}^{4} \{(y\frac{\mu}{\sigma_\epsilon})\frac{\partial \epsilon}{\partial x} + (y\frac{\mu}{\sigma_\epsilon})\frac{\partial \epsilon}{\partial y}\}_\alpha^n +$$

$$(c_{1\epsilon}\epsilon^n G^n - c_{2\epsilon}\rho^n \epsilon^{n^2})/k^n \tag{4.3}$$

In phase C, the Donor cell scheme was used to calculated the convection terms.

C. Wall Functions

The accurate solution of the boundary-layer equations for turbulent flows using models which evaluate the turbulent viscosity at all points within the flow requires that grid points be located within the viscous sublayer, $y^+ \leq 4.0$ for incompressible flow, and perhaps $y^+ \leq 1.0$ or 2.0 for flows in which a solution to the energy equation is also being obtained, where $y^+ = yu/\nu$. The use of equal grid spacing for the transverse coordinate would require several thousand grid points across

the boundary layer for a typical calculation at moderate Reynolds numbers. This at least provides motivation for considering ways to reduce the number of grid points required to span the boundary layer. the techniques which have been used successfully fall into three categories, use of wall functions, unequal grid spacing, and coordinate transformations. The wall function will be disscussed in this section. For many turbulent wall boundary layers the inner portion of the flow appears to have a "universal' character captured by the logarithmic "law of the wall". The inner region is a zone in which convective transport is relatively unimportment. The law of the wall can be roughly thought of as a solution to the boundary-layer momentum equation using Prandtl's mixing-length turbulence model when convective and pressure gradient terms are unimportment. In this approach, the law of the wall is usually assumed to be valid in the range $30 < y^+ < 200$ and the first computational point away from wall is located in this interval. The law of the wall equation was given by the logarithm form

$$\frac{u}{u_*} = \frac{1}{\kappa}\ln(\frac{yu_*}{\nu}) + B \tag{4.4}$$

where u is the tangential component of the fluid velocity at a perpendicular distance y from the wall, ν is the molecular kinematic viscosity, κ is von karman constant(in this study, the κ is set to 0.4), B is a constant that depends on wall roughness (we set $B = 5.5$ (smooth-wall)), and u_* is the shear speed, which is related to the wall shear stress τ_w and the fluid density ρ by $\tau_w = \rho u_*^2$.

In this equation, the u_* of equation (4.4) appears in both sides of the equation, which one would ordinarily have to solve iteratively. To avoid the inconvenience

this would entail we use instead an approximation obtained by replacing u_* in the argument of the logarithm by 1/7-law value u_*. The 1/7-law's equation (Hinze 1975) is given by

$$\frac{u}{u_*} = 8.3(\frac{u_* y}{\nu})^{1/7} \tag{4.5}$$

multiplied $yu_*/(8.3\nu)$ to both sides of equation (4.5) and took power 7/8, then the equation change to below

$$\frac{yu_*}{\nu} = 0.15(\frac{yu}{\nu})^{7/8} \tag{4.6}$$

substitute (4.6) into the right side of equation (4.4), the new equation was obtained

$$\frac{u}{u_*} = 0.75 + 2.19\ \ln(\frac{yu}{\nu}) \tag{4.7}$$

From this equation, it can be explicitly solved for u_*. The wall stress is then given by $\tau_w = \rho u_*^2$. If yu/ν (a Reynold's number based on y) is too small, the interested point lies in the laminar sublayer rather than the law-of-wall region. In this case, the laminar sublayer equation was given

$$\frac{u}{u_*} = (\frac{yu}{\nu})^{1/2} \tag{4.8}$$

The transition values between equation (4.7) and equation (4.8) is made at the point where they predicted the same u_*, which is $yu/\nu = 130.3$.

These equation are implemented numerically in the following way. Consider a typical cell adjacent to the wall, as shown in Figure 4.1. The shear stress τ_w for this cell is evaluated by setting

$$u = \frac{1}{2}[(u_L + u_R)^2 + (v_L + v_R)^2 + (w_L + w_R)^2]^{\frac{1}{2}}$$

$$y = \frac{1}{2}(h_L + h_R) \tag{4.9}$$

and $\nu = \mu_L/\rho$, where ρ is the density in the cell in question, and μ_L is evaluated at the temperature of the cell. Equation (4.7) and (4.8) incorporate two simplifying assumptions: (1) the normal velocity at points L and R is negligible, so that the tangential component may be replaced by the magnitude of the velocity, and (2) the lines connecting points L and R to their neighbors on the wall are approximately perpendicular to the wall. These values for u, y, and ν determine u_* and hence τ_w as already described.

With τ_w thus determined, the product $\tau_w A \Delta t$ gives the associated change in fluid momentum occurring on a time step (A is the wall area of the cell in question). Half of this change is apportioned to vertex L and the other half to vertex R. These changes are effected by multiplying all velocity components at each of these vertices by a single factor for that vertex, so that the directions of the velocity vectors do not change. (This procedure again relies on assumption (1) of the previous paragraph.) These factors are given by

$$F_L = 1 - \frac{1}{2}\frac{\tau_w A \Delta t}{M_L(u_L^2 + v_L^2 + w_L^2)^{\frac{1}{2}}}$$

$$F_R = 1 - \frac{1}{2}\frac{\tau_w A \Delta t}{M_R(u_R^2 + v_R^2 + w_R^2)^{\frac{1}{2}}} \tag{4.10}$$

where M_L and M_R are the vertex masses. If either of these factors comes out less than 0.3, It is replaced by 0.3 to prevent the velocities from changing by too large a factor on a single time step. It should be noted that these changes to the velocities at points L and R are only those due to the particular cell in question. A similar

change to the velocity at L will result from the wall cell to the left, and to the velocity at R from the wall cell on the right.

The wall function set for k is

$$k = \frac{u_*^2}{\sqrt{c_\mu}} \tag{4.11}$$

and for ϵ is

$$\epsilon = \frac{u_*^3}{\kappa y} \tag{4.12}$$

and the turbulent viscosity μ_t was calculated by equation (2.11).

D. Initial Conditions

At the inlet of the calculation domain, all dependent variables have to be specified. The k profile may be estimated from the measurements. In general, k is specified as a percentage of the inlet mean square velocity.

$$k_{in} = 0.003 \times u_{in}^2 \tag{4.13}$$

The inlet profile for ϵ has to be assumed, since no measurements are available. It is specified as

$$\epsilon_{in} = c_\mu k_{in}^{3/2}/(0.03D/2) \tag{4.14}$$

where D is characteristic length at the inlet and $c_\mu = 0.09$.

From this two initial values, the turbulent viscosity μ_t can be calculated by the equation (2.11).

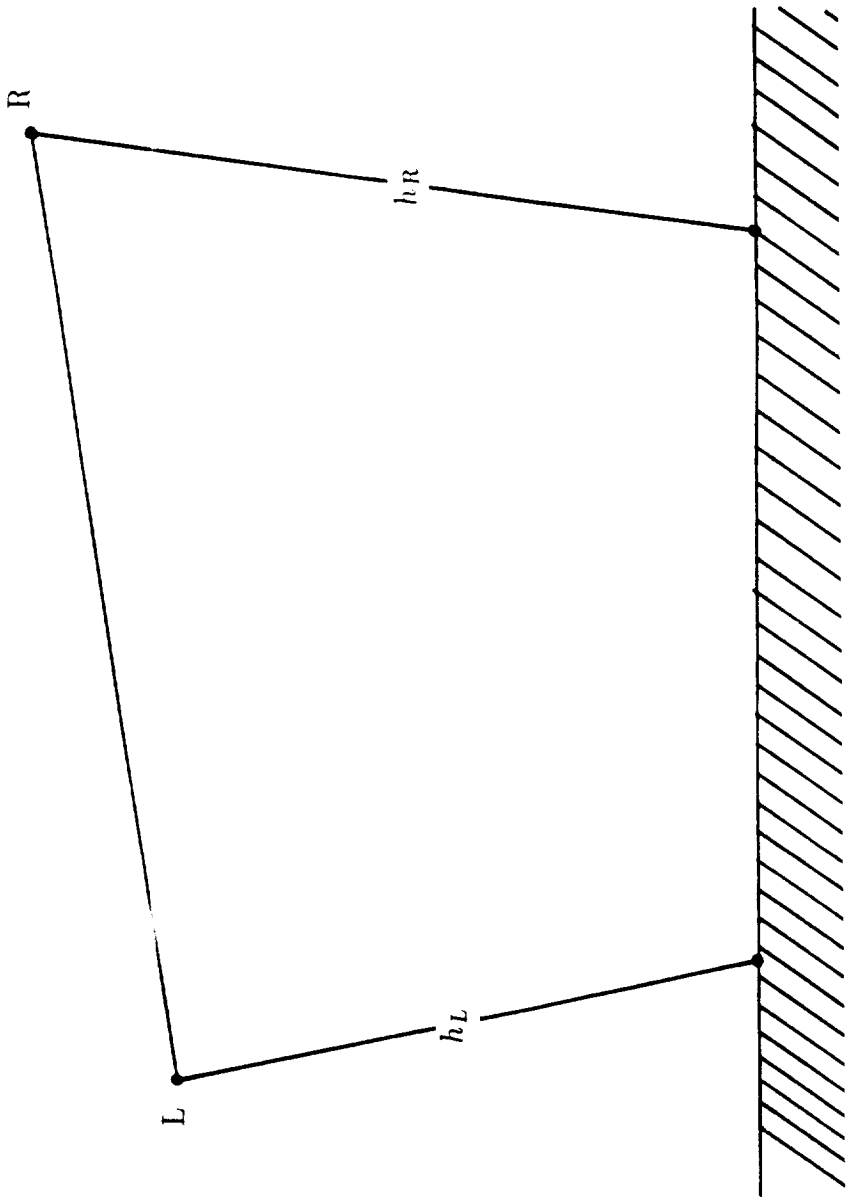

Figure 4. 1 Typical Cell used for Wall Function

CHAPTER V RESULTS AND DISCUSSION

For the purpose of code validation and testing, several benchmark problems with available analytical and experimental data have been chosen. The first case is the Burger's equation with complex geometries and boundaries. Next, the laminar and turbulent pipe flows are calculated. Finally, a confined coaxial jet flow relevant to combustor design is calculated.

A. Solution Of Burger's Equation With Complex Geometries And Boundaries

The purpose of this problem is to test the capability of the ALE-ICE scheme for handling complex geometries and boundaries. The Burger's equation with mixed Neumann and Dirchlet boundaries are chosen to test the ALE-ICE scheme.

The Burger s equations for the unsteady incompressible flow may be written as

$$\frac{\partial u}{\partial t} + u\frac{\partial u}{\partial x} + v\frac{\partial u}{\partial y} = \nu(\frac{\partial^2 u}{\partial^2 x} + \frac{\partial^2 u}{\partial^2 y}) + f_x$$
$$\frac{\partial v}{\partial t} + u\frac{\partial v}{\partial x} + v\frac{\partial v}{\partial y} = \nu(\frac{\partial^2 v}{\partial^2 x} + \frac{\partial^2 v}{\partial^2 y}) + f_y \qquad (5.1)$$

where

$$f_x = \frac{1}{1+t}(x^2 + 2xy - \frac{1}{1+t}) + 3x^3y^2 - 2\nu y$$

$$f_y = \frac{1}{1+t}(y^2 + 2xy - \frac{1}{1+t}) + 3x^2y^3 - 2\nu x$$

with the Neumann boundary conditions and the Dirchlet boundary conditions specified according to Figure 5.1. The Neumann boundary conditions are specified:

$$\frac{\partial u}{\partial x} = 2xy$$

$$\frac{\partial u}{\partial y} = x^2$$

$$\frac{\partial v}{\partial x} = y^2$$

$$\frac{\partial v}{\partial y} = 2xy \tag{5.2}$$

The solution will be compared with the exact solution

$$u = \frac{1}{1+t} + x^2 y$$

$$v = \frac{1}{1+t} + xy^2 \tag{5.3}$$

First, grid independence studies were carried out by using three grids : $4 \times 10, 8 \times 20$ and 16×40. The case considered was $\nu = 1$ and times step was set rather small to reduce any instability. The total r.m.s. errors, which was defined as sum of the pointwise r.m.s. error

$$[\|e\|] = \{\sum (u_i - \overline{u}_i)^2 / \sum u_i^2\}^{1/2}] \tag{5.4}$$

were plotted vs time on Figure 5.2. Both 8×20 and 16×40 reaches asymptotic values of 7%, and since only the long- time behaviors are compared the rest of the results are shown using the 8×20 grid. Effect of viscosity on the calculated results is shown on Figure 5.3. As expected, as Reynolds number increases (ν decreases), convection term dominates and due to the upwind scheme for the

convection term approximation, the total r.m.s. errors increases. Typical results in terms of pointwise errors are shown in Figure 5.4 and Table 5.1. For areas closed to non-orthogonal grids and Neumann's B.C.'s, there appear to have less accurate results (Lee et al. 1989). This points to the further development in terms of flux calculations in the ALE-ICE method for irregular grids and Neumann Boundary condition implementations.

B. Laminar Pipe Flow

The second testing case is a laminar pipe flow. The pseudocompressibility method described in Chapter 3 was used for the incompressible flow case. This method has also been used in Rogers et al. (1987), Liang et al. (1985) and Nichols et al. (1980) for incompressible flows.

The analytical solutions of laminar pipe flows were given in Bird et al. (1960). The calculated results will be compared with the analytical solution. The velocity distribution in the fully developed region was given by

$$U_x = 2\ U_b\ [1 - (\frac{x}{R})^2] \tag{5.5}$$

where U_x is the longitudinal velocity, U_b is the bulk velocity and R is the radius of the pipe.

The Reynolds number ($Re = DU_b/\nu$) of 1,000 was carried out for laminar flows in which D is the pipe diameter and ν is the viscosity. In Figure 5.5, 5.6 different β values (ρc^2) were tried to find the optimal performance. For β around 5 the solutions obtained were optimal. Next, grid independence studies were carried out by using 11 x 81, 21 x 81 and 31 x 81 grids. In Figure 5.7, 5.8 fully developed

and developing profiles show that 21 x 81 and 31 x 81 grids converged to the same solutions and compare well with the analytical solution velocity within about .8 % errors. The calculation was done by assuming the plug profile at the pipe inlet and the calculation domain was 60 in pipe diameter. Fully developed (Figure 5.9) and developing (Figure 5.10) data compared to analytical solution velocity is only .75 % errors in 21 x 81 case. In this section, each case runs about 17,000 cycles and each cycle uses .7 second on CRAY-XMP. This simulation will give some suggestion to the ALE-ICE scheme's future works and will help the next test case for turbulent flows.

C. Turbulent Pipe Flow

Most turbulence models have been tested and/or developed using fully developed pipe flow conditions, and this testing will be made in this study. As recommended by Martinuzzi and Pollard (1989), the calculated results are compared to one another, and, for the sake of placing the calculations in perspective, they are compared to various data sets that appear in the literature. A single data set has not been used because, in the authors' opinion, a reliable, well-documented data set does not exist due to back of providing detailed inlet conditions. As a results, the data sets of Richman and Azad (1973), Lawn (1971) and Nikuradse (1932) will be compared with the calculation results. From Martinuzzi and Pollard (1989) recommendation, the Re =10,000 and Re =100,000 will be used in this study.

Calculation grids 21 x 81, 31 x 81 for Re =10,000 and 51 x 81, 61 x 81 and 71 x 81 for Re =100,000 were used by grid independence study. The plug flow condition

was used at the inlet. The β value for 21 x 81 and 31 x 81 was 500 and for 51 x 81, 61 x 81 and 71 x 81 grids was 5 000. The calculation domain was 80 in the pipe diameter. Empirical relationships are used to assign entrance values to k and ϵ; that is, $k = 0.03\ U_b^2$ for Re =10,000, $k = 0.03\ U_b^2$ for Re = 100,000 and $\epsilon = (C_\mu k^{\frac{3}{2}}/0.03/R)$.

In Figure 5.11, the fully developing axial velocity profiles normalized by the inlet velocity, at Re =10,000, was presented. Figure 5.12, the fully developed velocity profiles are compared with those data of Nikuradse. The fully developed profiles at Re =10,000 for $u^+ = u/u_*$ vs y^+ is shown in Figure 5.13, the slopes are generally well reproduced, but the absolute values of the calculations tend to overpredict the data of Nikuradse (1932). The developing velocity profiles for Re =100,000 are shown in Figure 5.14 with the data of Richman and Azad (1973). The differences are negligible. The fully developed axial velocity profiles at Figure 5.15, at Re =100,000, are compared with those data of Richman and Azad (1973). The agreement between experimental data and calculations is poorer close to the wall boundary. This can be further seen from Figure 5.16 where the mean velocity profile is plotted using the wall coordinate. Using the 1/7-th law wall function forced the first grid calculation results to match the logarithm wall. Due to the poor turbulence model capability for strong shear flows, the predictions deviate significantly away from the wall.

The distribution of the turbulence kinetic energy in the fully developed region for Reynolds number of 10,000 is overpredicted (Figure 5.17) and is underpredicted (Figure 5.18) for Re =100,000 as compared to Lawn's experimented data.

It should be noted that the 1/7-th law wall function used in there calculations is only valid for fully developed turbulent pipe flows. This assumption is incapable of modeling developing regions and separated regions as will be seen in the next test case. The use of the 1/7-th law wall function is probably responsible for the poor performance of the $k-\epsilon$ model toward the wall regions as implemented in this study.

D. The Coaxial Jet Flow

The Space Shuttle Main Engine (SSME) high pressure fuel preburner consists of 264 coaxial injector elements injecting gaseous hydrogen and liquid oxygen into a large cylindrical chamber. The ARICC code was originally developed to simulate these types of flowfield. The outer wall is a free-slip boundary that corresponds to the imaginary symmetry surfaces of a streamtube whose diameter is determined based on the average cross-sectional area available to each injector element (Liang et al. 1986a). This ability is deemed necessary for the simulation of the confined coaxial jet flows. Owen's turbulent recirculating jet flows (1976) will be tested in this study.

Owen's turbulent recirculating jet flows (1976) is a complex one consisting of large recirculating zones. It is a confined coaxial jet flow with high velocity ratio between annular jet and central jet, and a central toroidal recirculation zone is formed due to the imbalance of the mass flow between the central and annular jets. The sudden expansion of annular jet results in a severe adverse pressure gradient. When this pressure gradient is too strong for the low momentum central jet, a

central toroidal recirculation zone results in addition to the corner recirculation zone.

In an effort to provide such data and also to understand the nature of the flow in a coaxial jet flow configuration of interest to combustor designers, Owen carried out detailed turbulence measurements using LDA. The Owen's experimental configuration (reproduced in Figure 5.19) consist of a 2.5 in (6.35 cm) central jet surrounded by a 3.5 in (8.89 cm) annular jet. The jets discharge into a 5 in (12.7 cm) diameter chamber 48 in (121.9 cm) long. The outer and inner peak velocities were 96.0 (29.26) and 8.0 (2.44) fps (m/sec) corresponding to Reynolds numbers based on respective jet diameters of 1.5 and 0.08 $\times$ 10^5. Inflow profiles were not reported.

Sturgess, et al. (1983), Syed and Sturgess (1980), Novick, et al. (1979) predicted the confined coaxial jet flow corresponding to the experimental conditions of Owen's (1976) with $k-\epsilon$ turbulence model. None of these predictions produced the shape, size, and location of the important central toroidal recirculation zone correctly (Nallasamy 1987). The length of the central recirculating zone was severely underpredicted by about 40 percent. As concluded by Nallasamy (1987), the corner and central recirculation zones are very sensitive to the central jet exit geometry.

Computations for this case were made using ARICC code with 21 x 81 and 31 x 81 unstructured grids, shown in Figure 5.20. The calculation domain was 12 times of the diameter of the chamber and extended 4 inches for inlet flow. The inner jet is 2.5 inches, the outer jet is 3.5 inches and the chamber is 5.0 inches. The Reynolds number for inner jet is 8000 and for outer jet is 15,000; $Re = DU_b/\nu$, where D

is the jet correspondence diameter and U_b is the bulk velocity for correspondence jets. ν is the kinematic viscosity. The inlet values for k is $0.003 \times U_b^2$ and for ϵ is $C_\mu k^{\frac{3}{2}}/0.03/R$. Computations were made with the subgrid and the $k-\epsilon$ model.

Figure 5.21 shows the comparisons of the centerline mean axial velocity profiles and the measured values. The $k-\epsilon$ model prediction is good up to 2.0 D and the subgrid model only within 0.5 D. Beyond those the predicted value are smaller than the measured one. The mean velocity profiles predicted by the $k-\epsilon$ model and subgrid model compared to the measured values are illustrated in Figure 5.22, 5.23. The predicted mean velocity profiles of $k-\epsilon$ model are in good agreement with the data, but subgrid model are not. Between x/D=0.25 and x/D=1.8, some differences between the data and the predictions are seen. However, the overall predictions of $k-\epsilon$ model are in good agreement with data in the recirculation zone. The $k-\epsilon$ model predictions for r.m.s. velocity fluctuation and the data are shown in Figure 5.24. The prediction is very close to the data. Figure 5.25 shows the streamline patterns, subgrid model center recirculating zone is larger than that of $k-\epsilon$ model's. The $k-\epsilon$ model shows a better representation of the experimental data. For corner recirculating zones, $k-\epsilon$ model also shows good predictions

Figure 5.26 shows the transient behavior of ARICC code. As seen from those profiles, they are not real transient results. Equation 3.22 indicated that the continuity equation can only be satisfied steady state was reached From this point of view, the transient results are not time-accurate and only represent intermediate transient to the final steady state results.

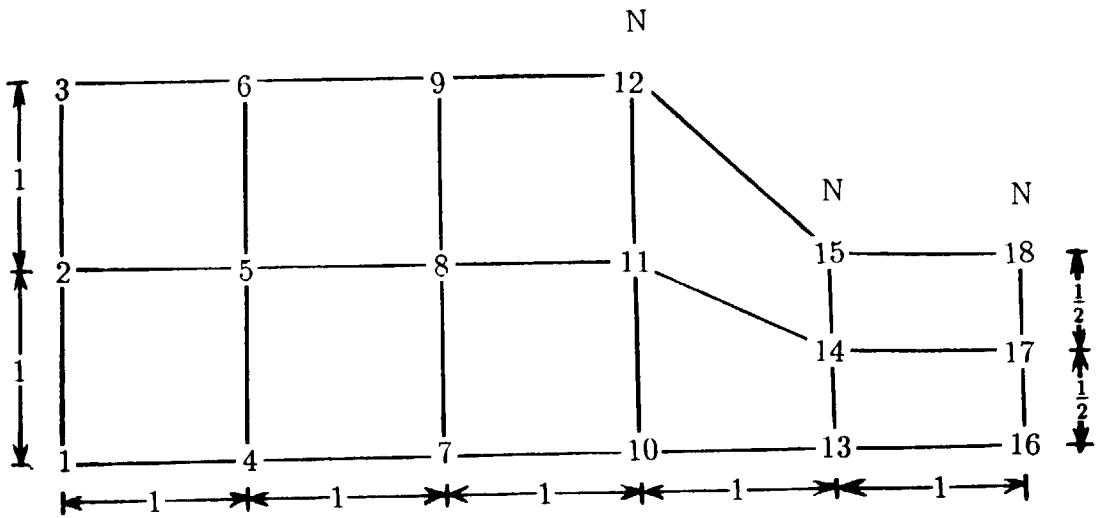

Figure 5. 1 Complex Geometries Grid used in Burger's Equations

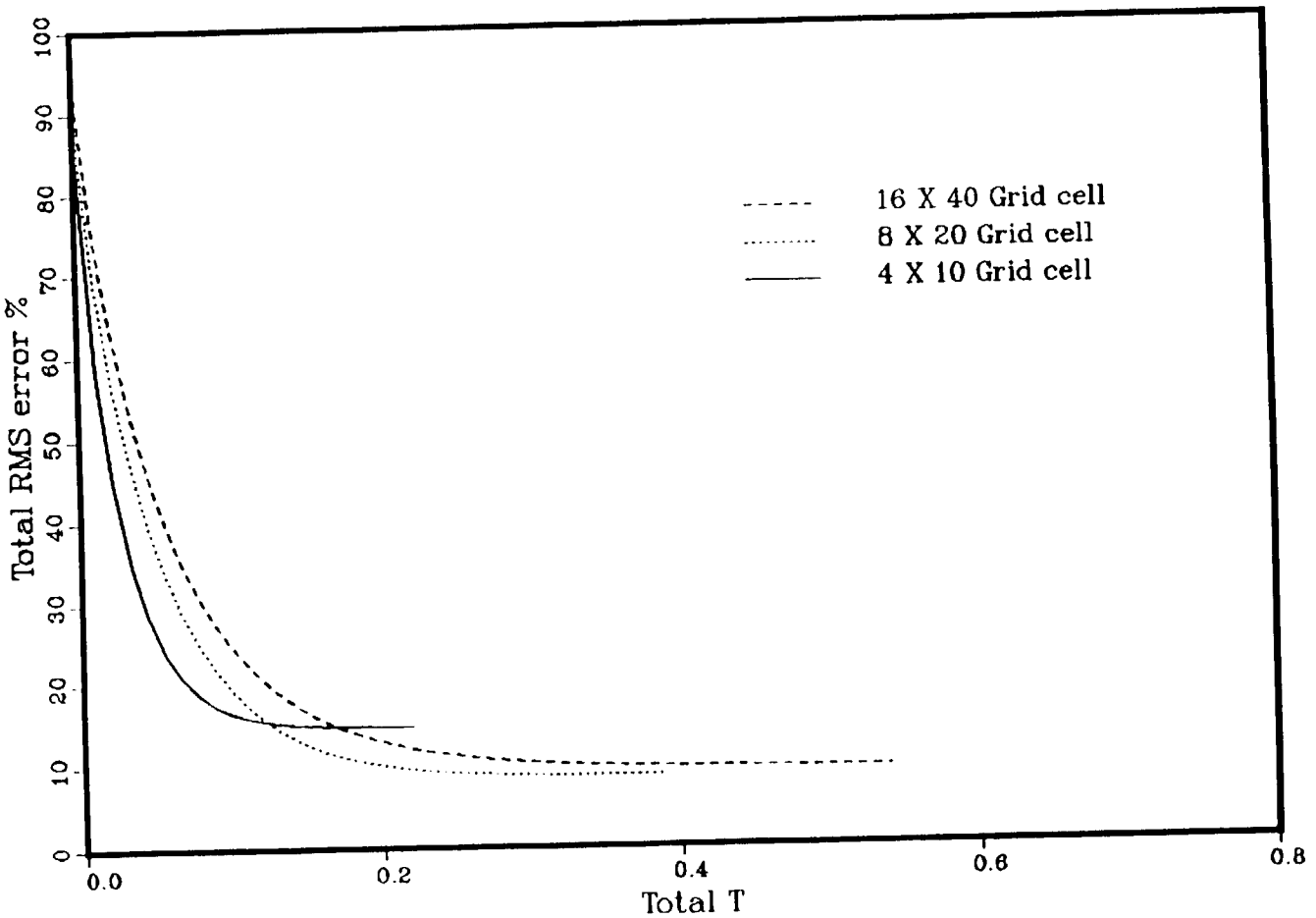

Figure 5. 2 Total R.M.S. Error for Grid Indenpendent Study

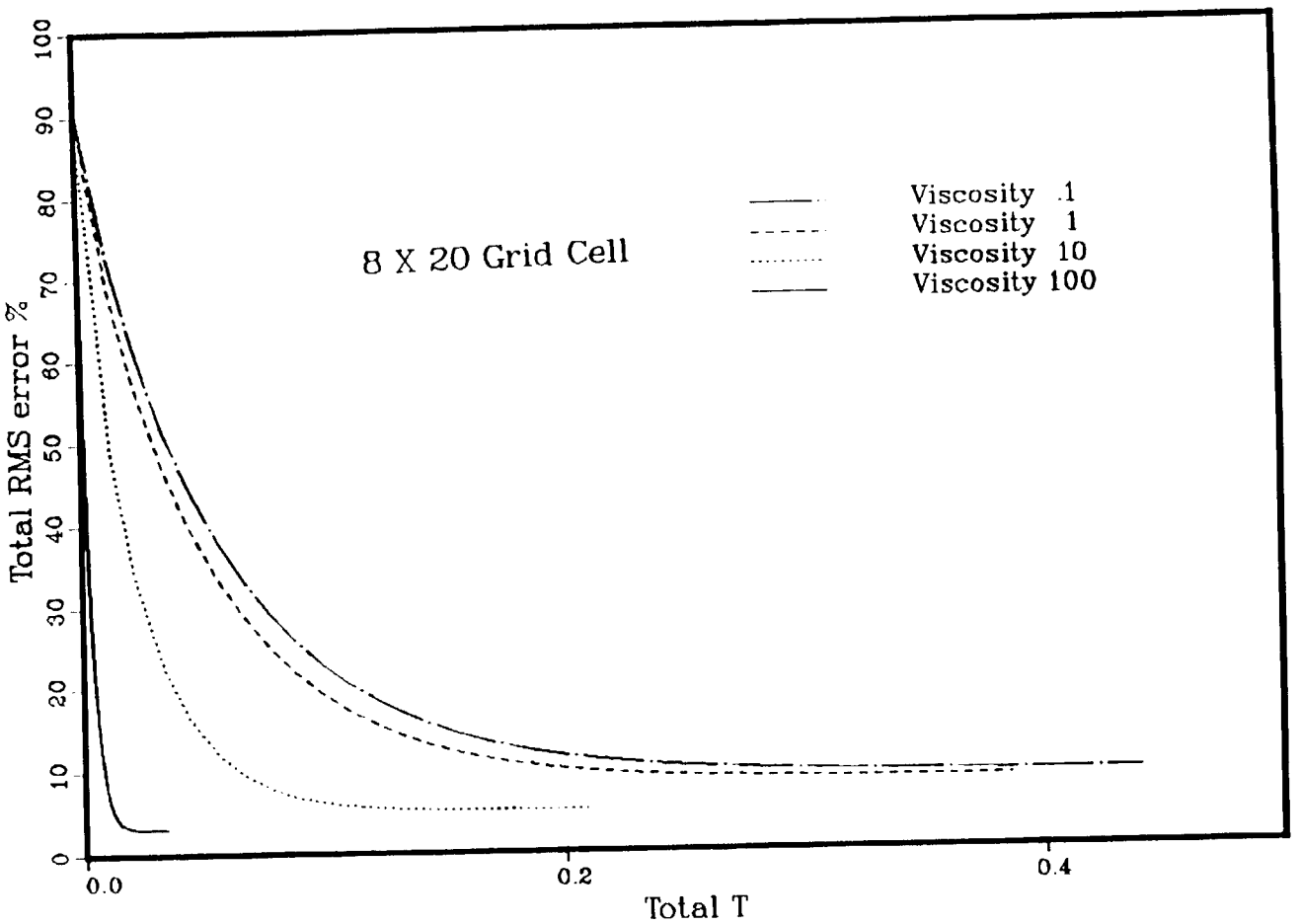

Figure 5. 3 Total R.M.S. Error for Different Viscosity

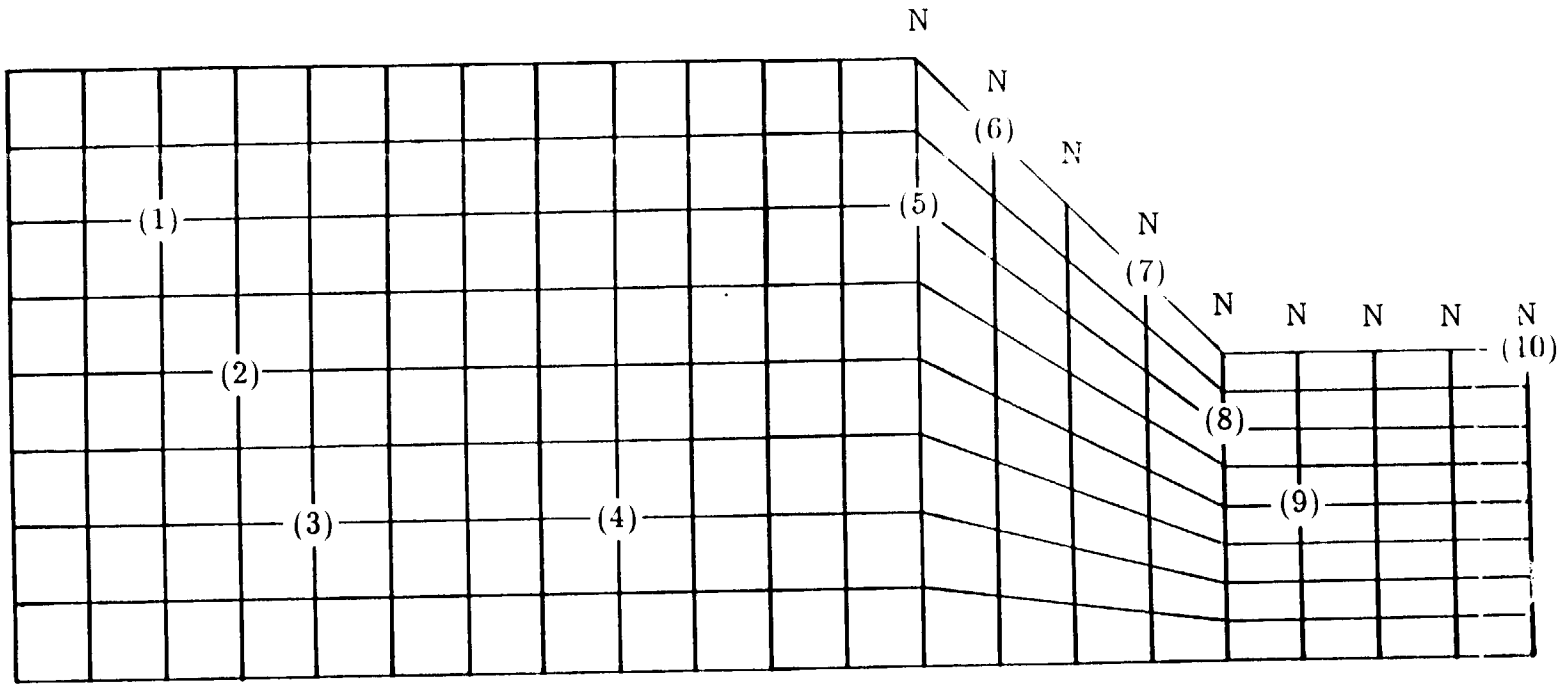

Figure 5. 4 8 × 20 Grid Cell

Table 5. 1 Values for Figure 5.4

	predict		exact		error rms	
	u	v	u	v	u	v
(1)	1.96	1.22	1.96	1.21	4.9E-5	9.18E-5
(2)	1.59	1.39	1.58	1.39	1.12E-4	2.73E-5
(3)	1.108	1.32	1.083	1.33	1.85E-4	9.06E-5
(4)	1.34	2.71	1.33	2.83	6.7E-5	9.6E-4
(5)	6.96	13.15	7.58	14.33	4.6E-3	8.9E-3
(6)	9.93	17.90	10.80	19.30	6.4E-3	1.06E-2
(7)	6.23	17.09	6.69	18.40	3.4E-3	9.9E-3
(8)	2.92	12.27	3.08	12.80	1.24E-3	4.24E-3
(9)	1.86	10.66	1.96	10.95	7.61E-4	2.28E-3
(10)	5.75	25.54	5.83	25.833	6.2E-4	2.18E-3

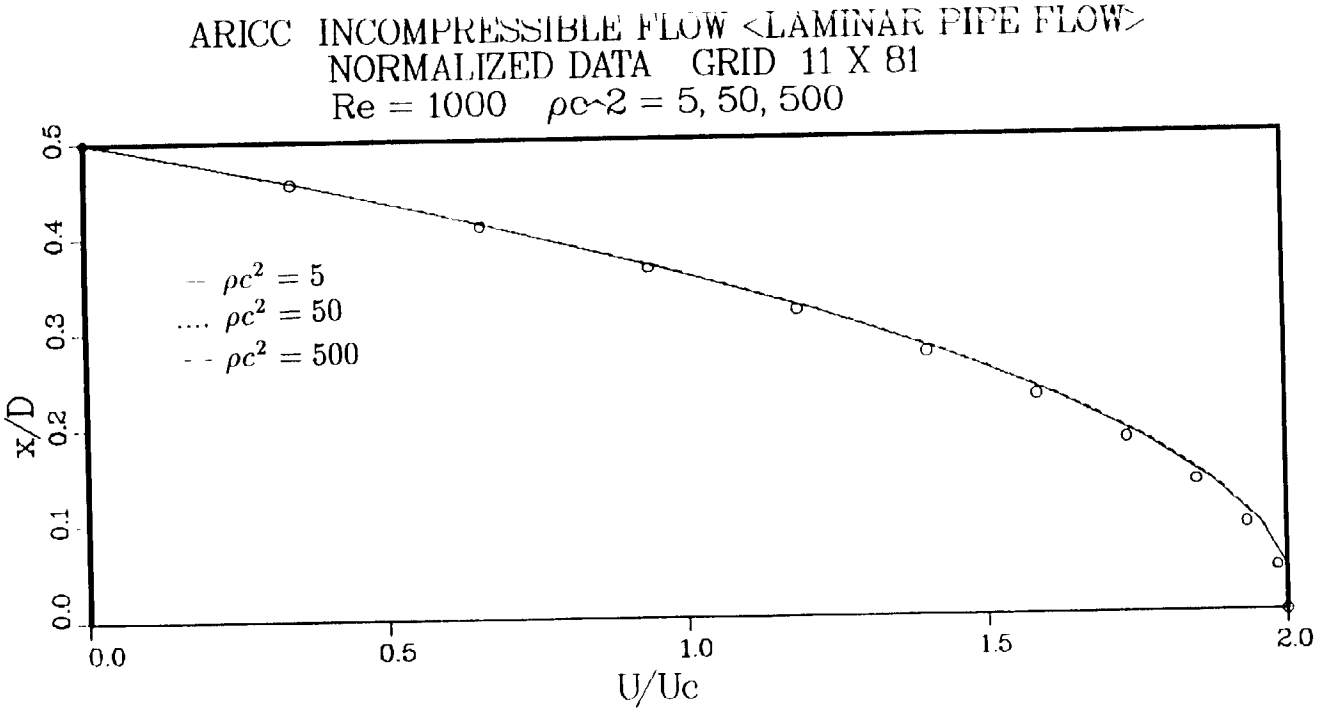

Figure 5. 5 Fully Developed Velocity Profiles with Different β Number

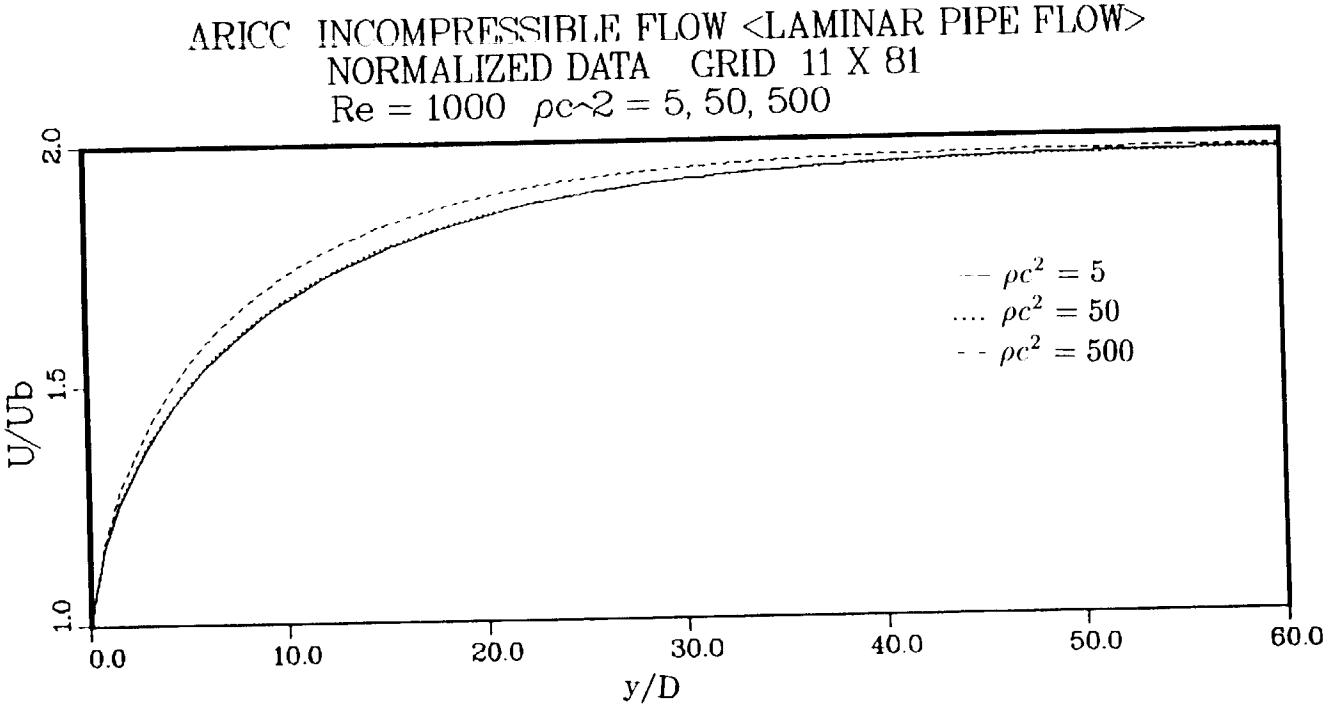

Figure 5. 6 Development of Centerline Velocity for Different β Values, $\beta = 5, 50, 500$

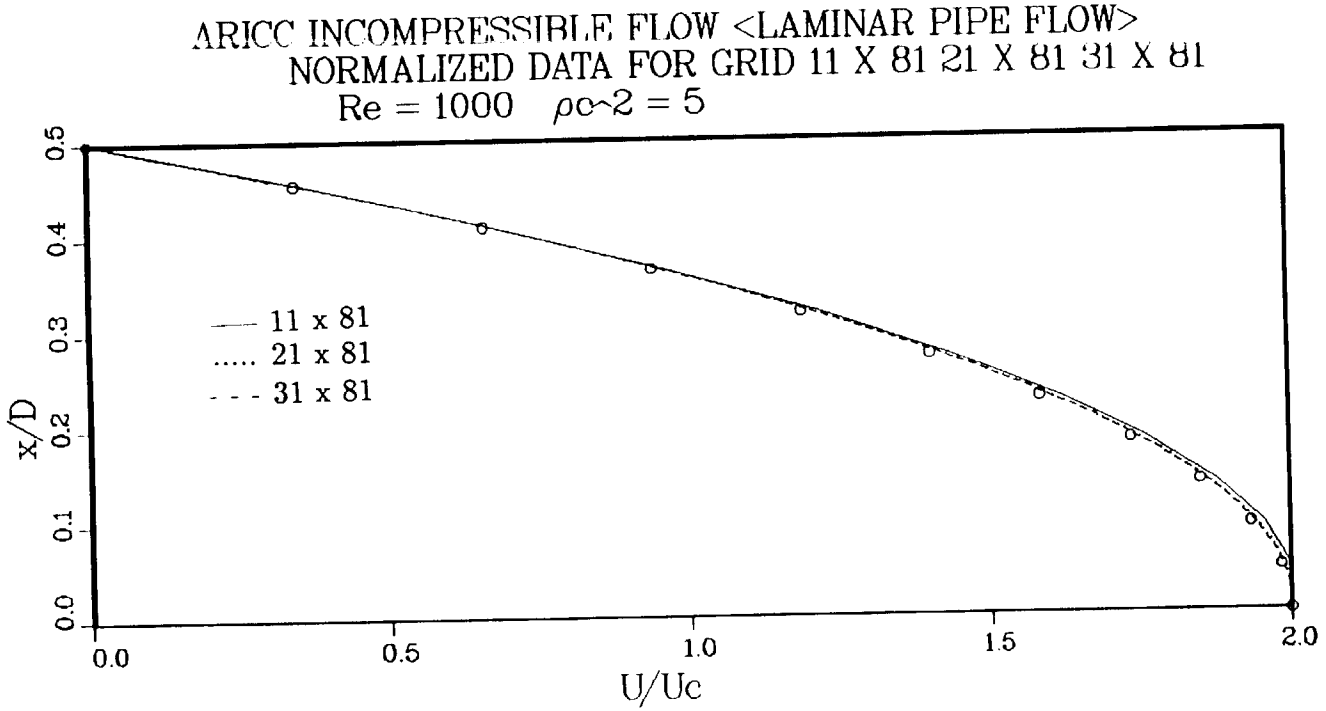

Figure 5. 7 Grid Indenpent Study 11 × 81, 21 × 81, 31 × 81

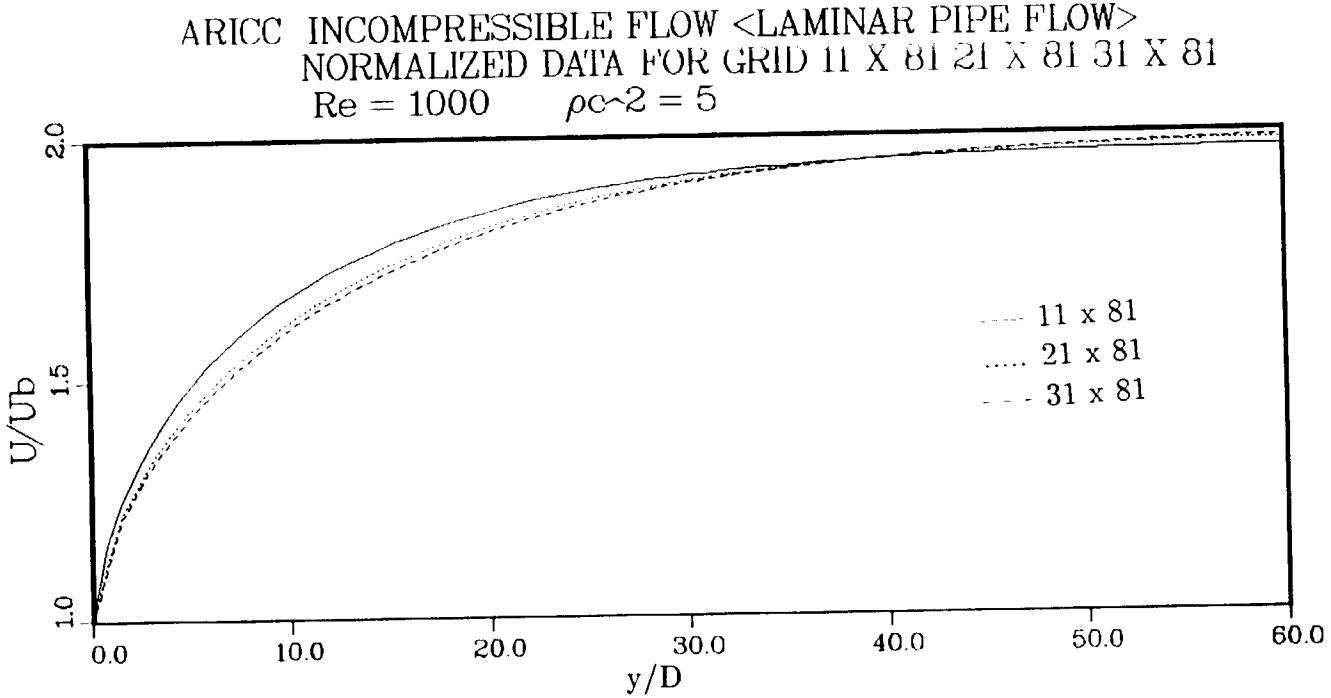

Figure 5. 8 Axial Velocity Profiles for Normalized Data

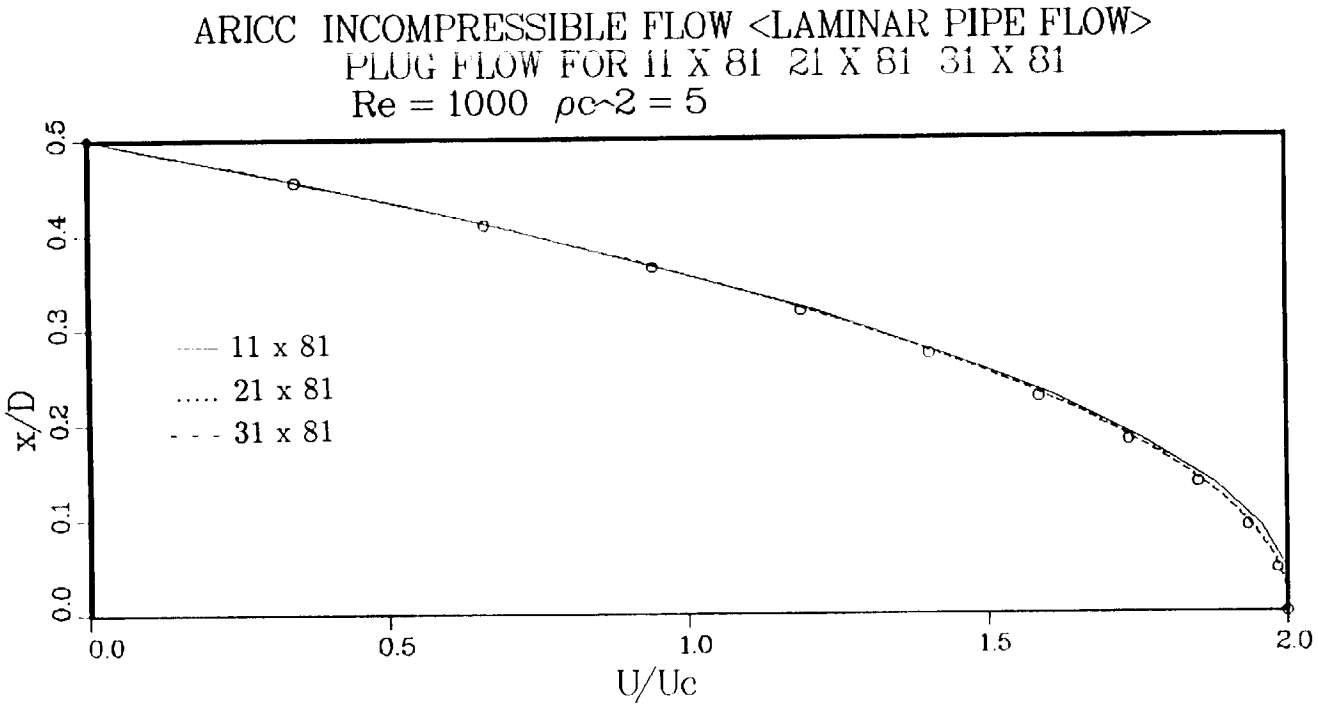

Figure 5. 9 Fully Developed Velocity Profiles

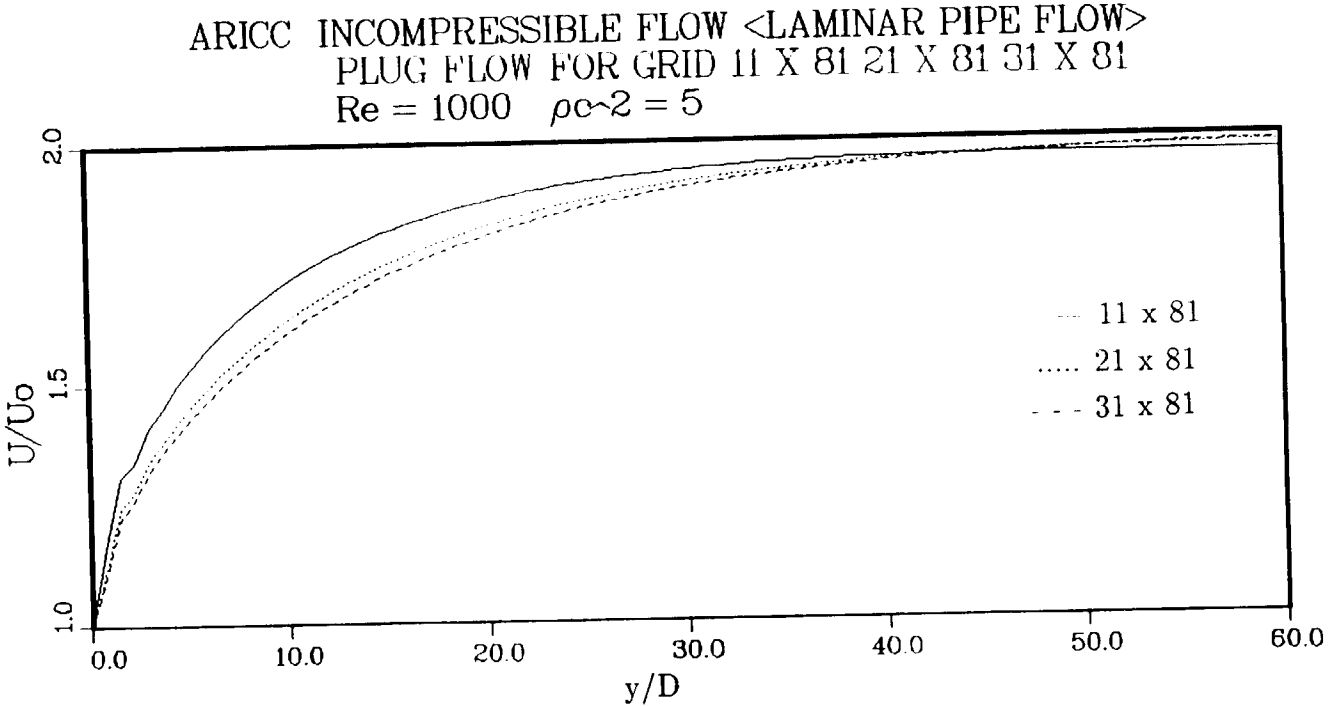

Figure 5.10 Axial Velocity Profiles

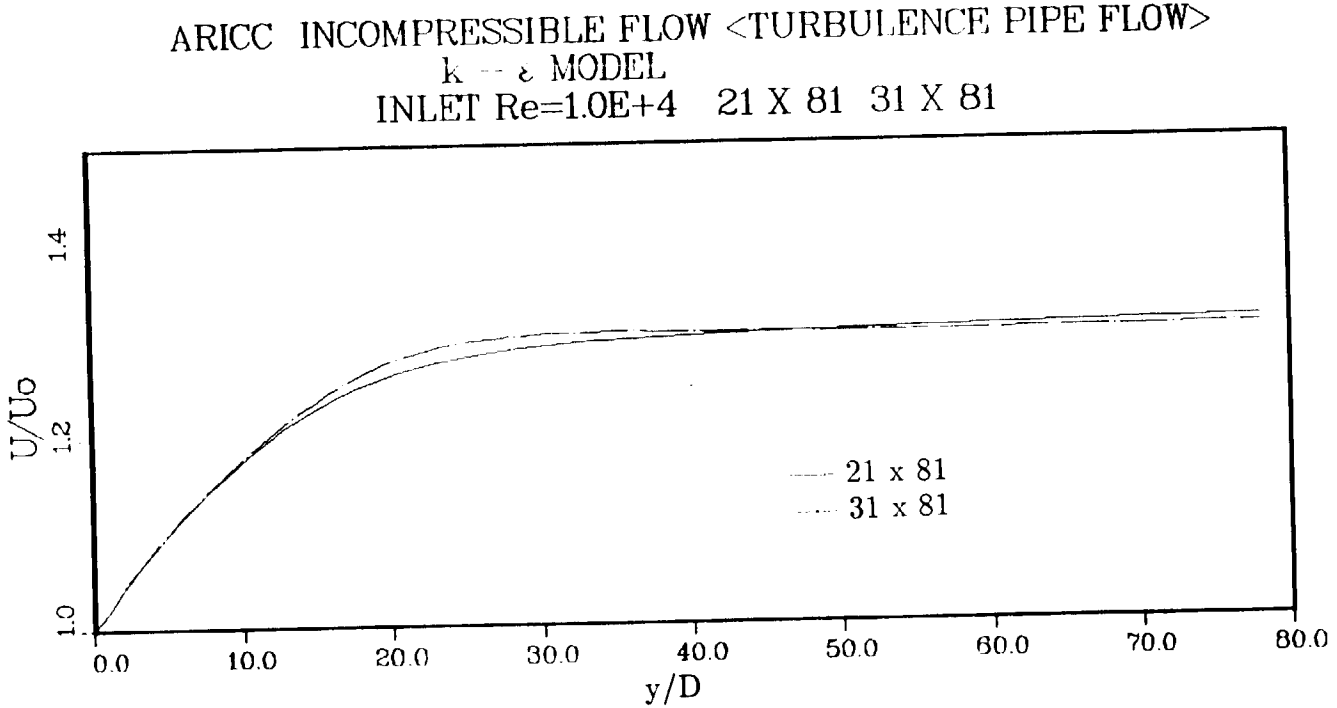

Figure 5.11 Development of Centerlines Velocity Profiles for Re =10,000

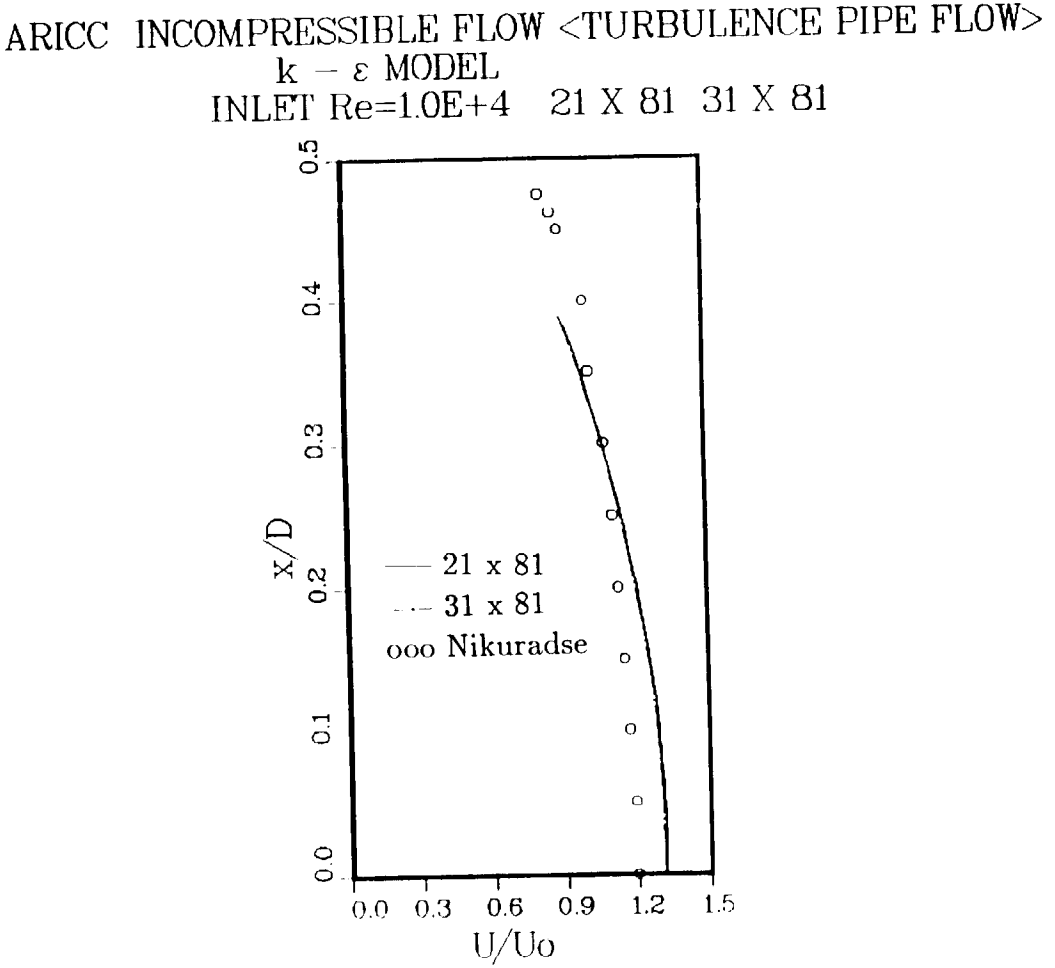

Figure 5.12 Axial Velocity Profile for Re =10,000

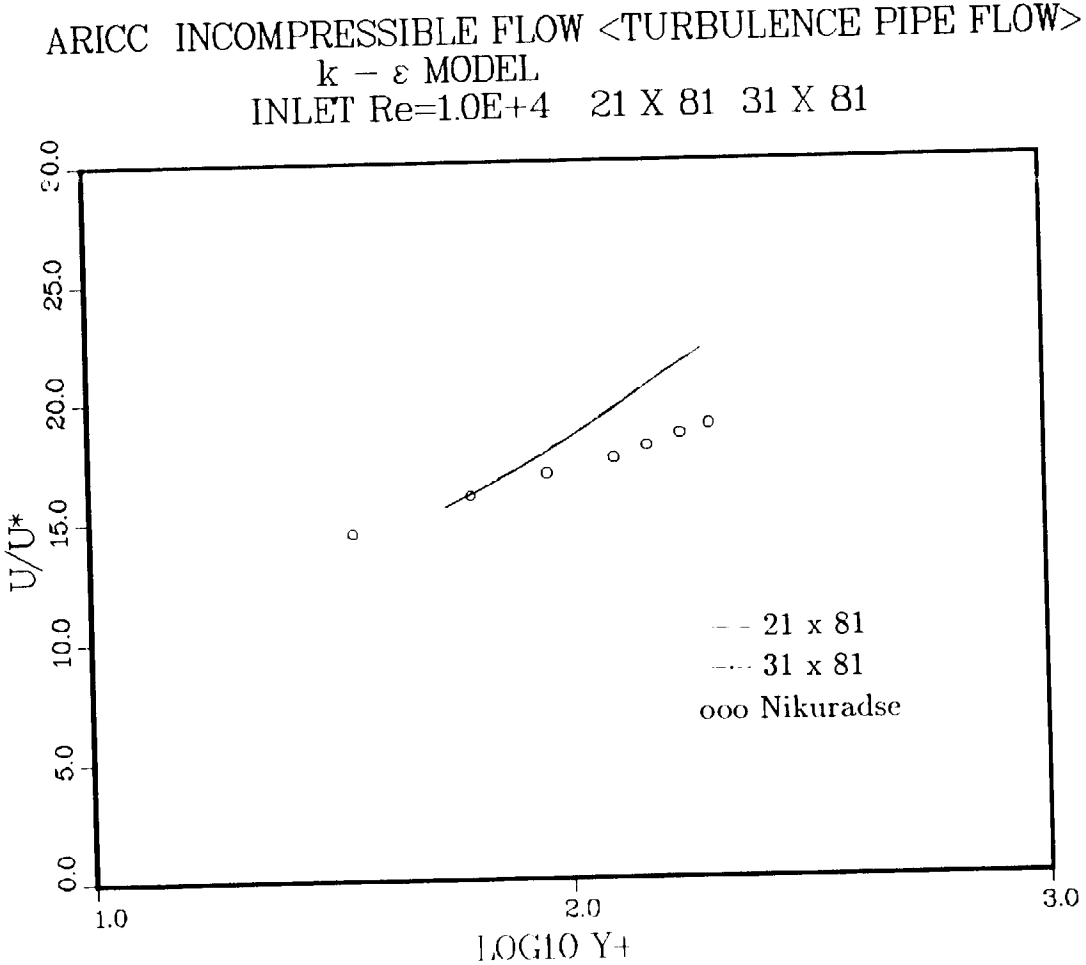

Figure 5.13 u^+ vs y^+ at y/D=80 for Re =10,000

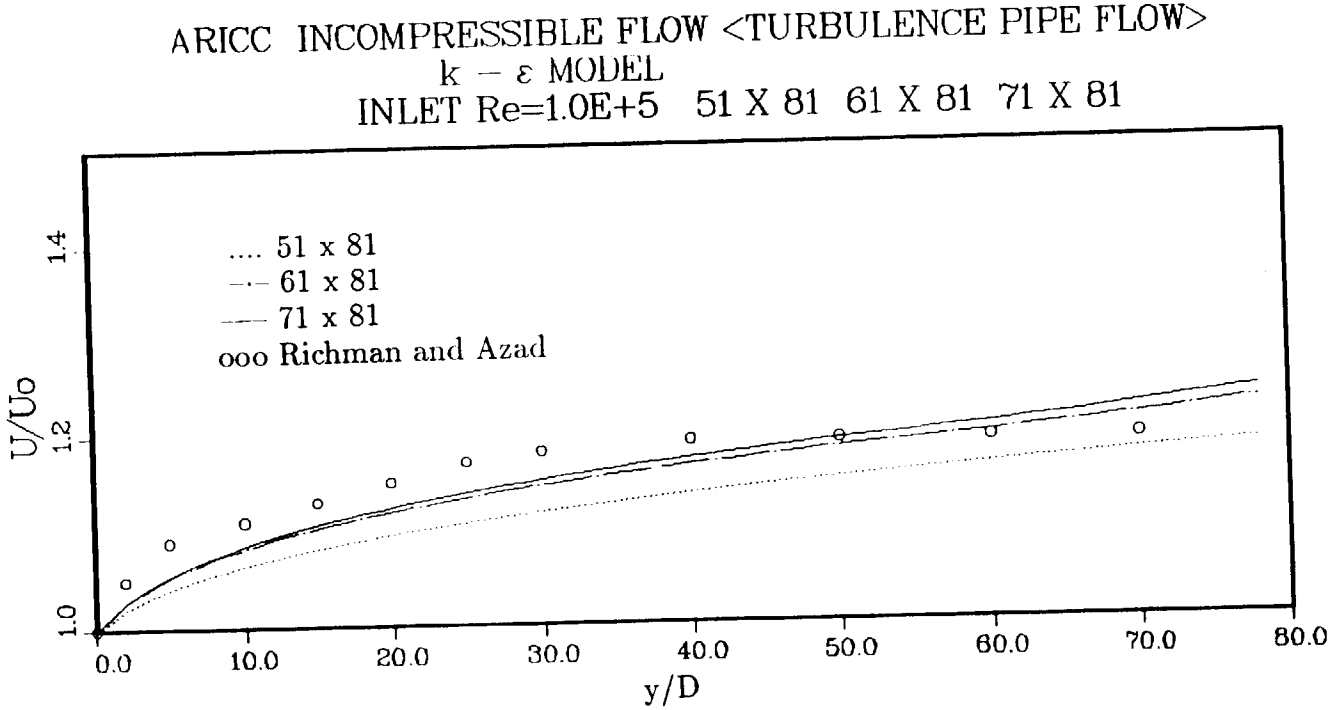

Figure 5.14 Development of Centerline Velocity Profiles for Re =100,000

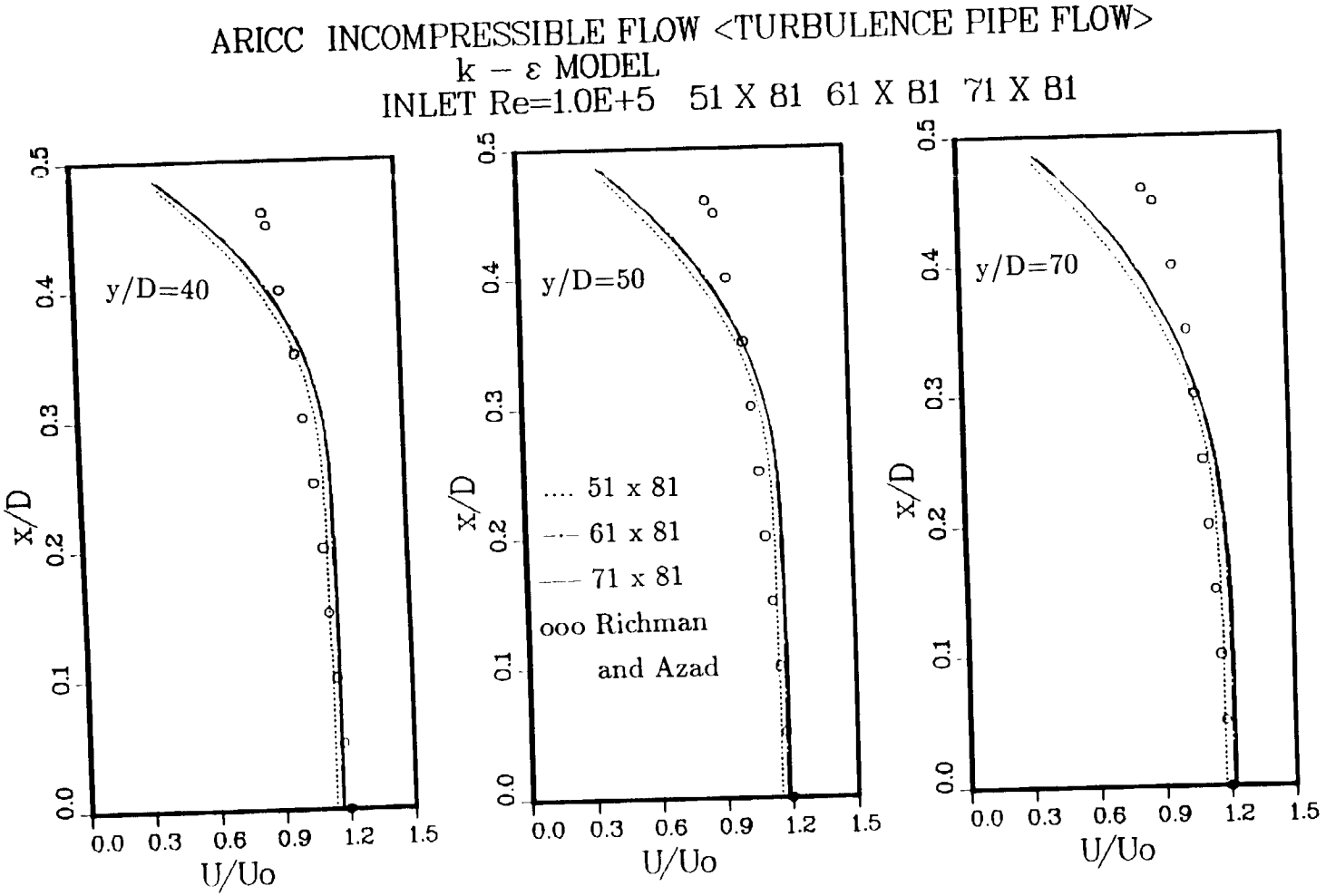

Figure 5.15 Variation of Axial Velocity with y/D=40, 50, 70 for Re =100,000

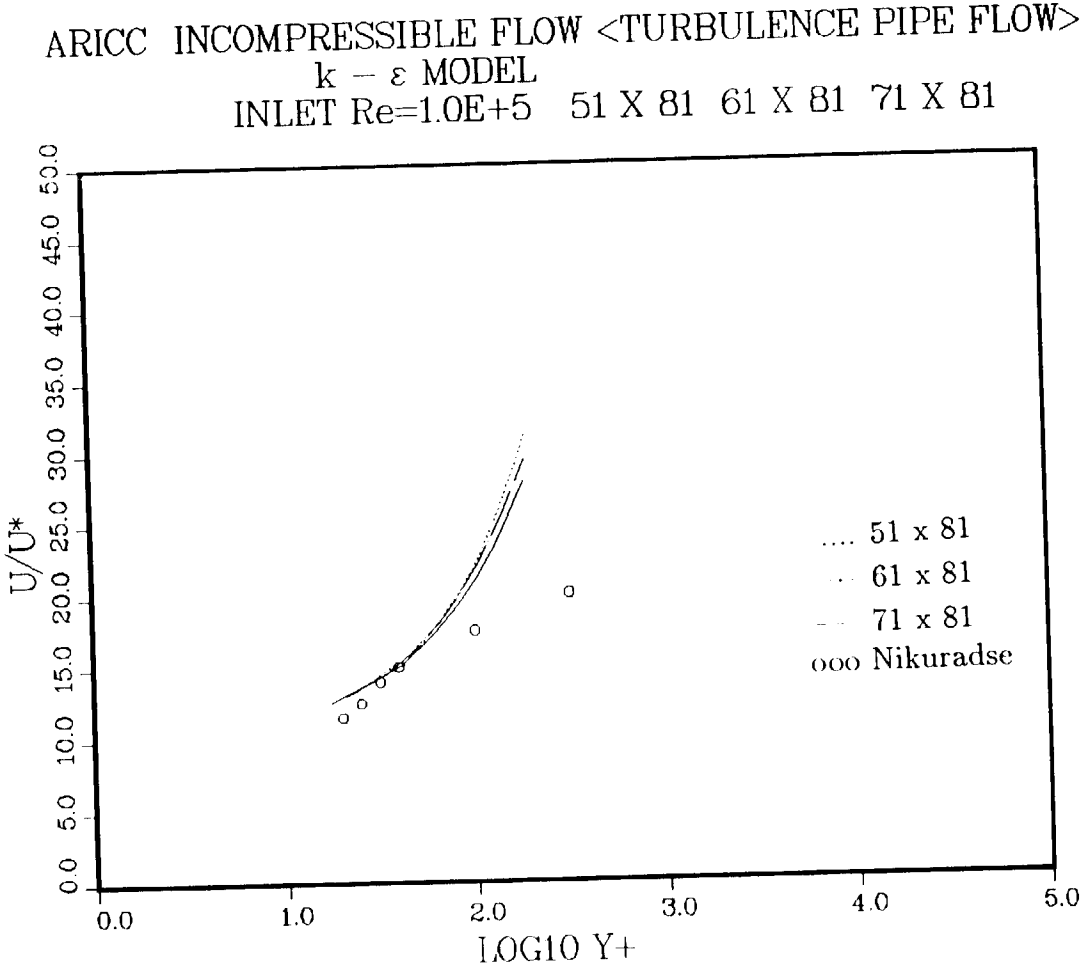

Figure 5.16 u^+ vs y^+ at y/D=80 for Re =100,000

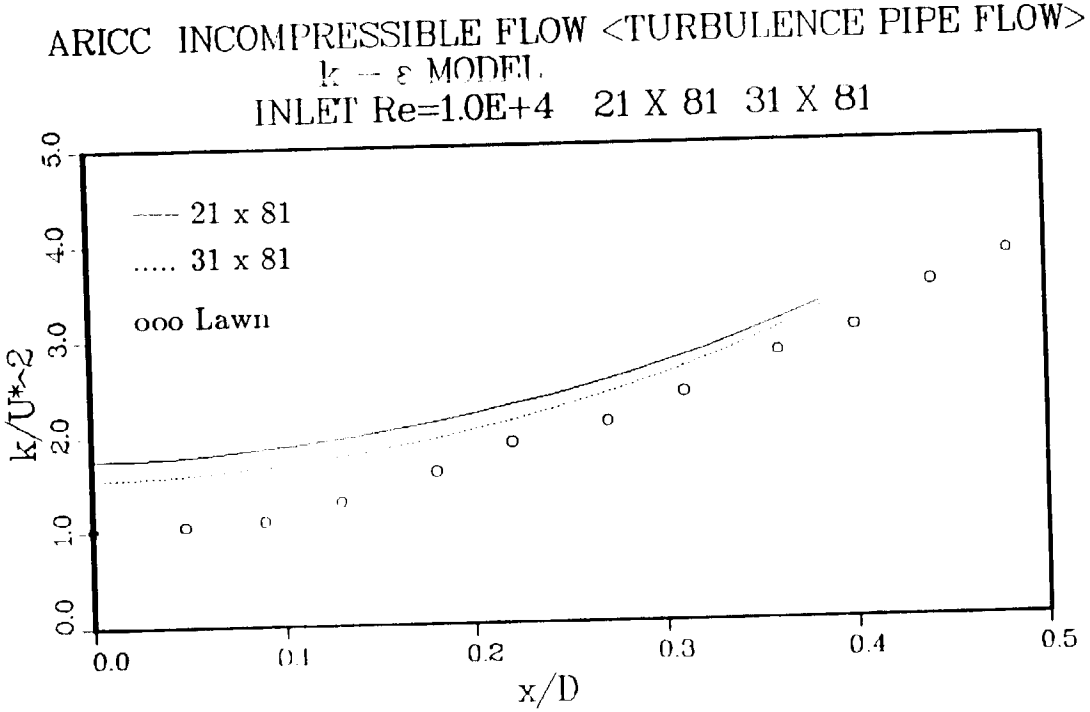

Figure 5.17 Turbulence Kinetic Energy vs x/D at y/D=80 for Re =10,000

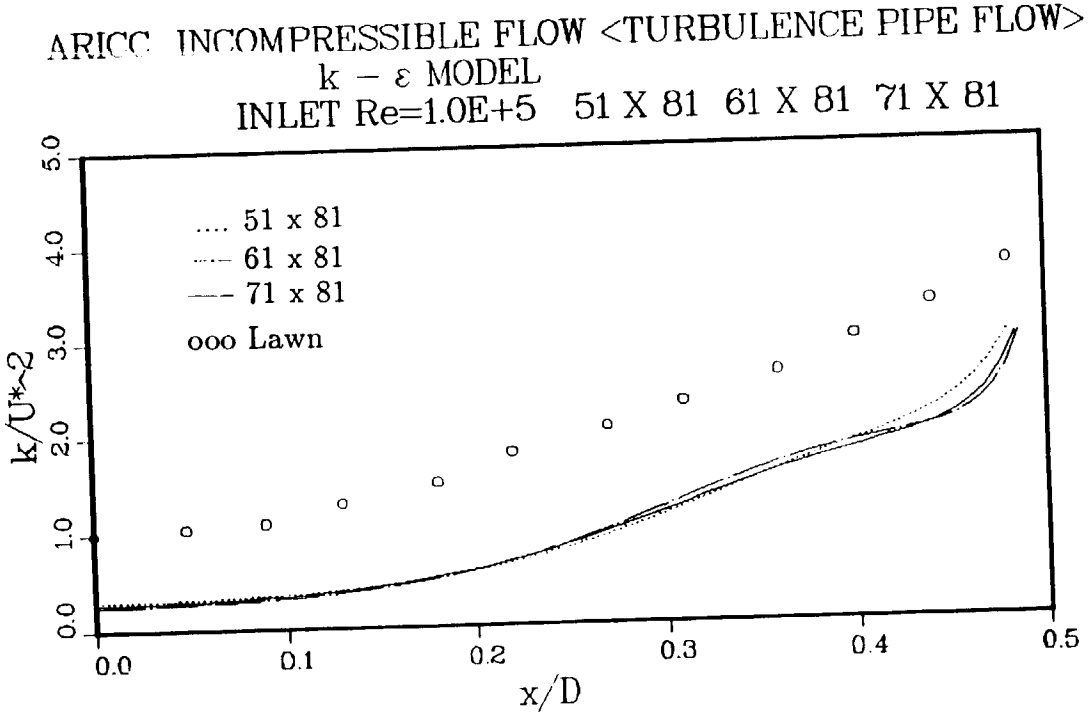

Figure 5.18 Turbulence Kinetic Energy vs x/D at y/D=80 for Re =100,000

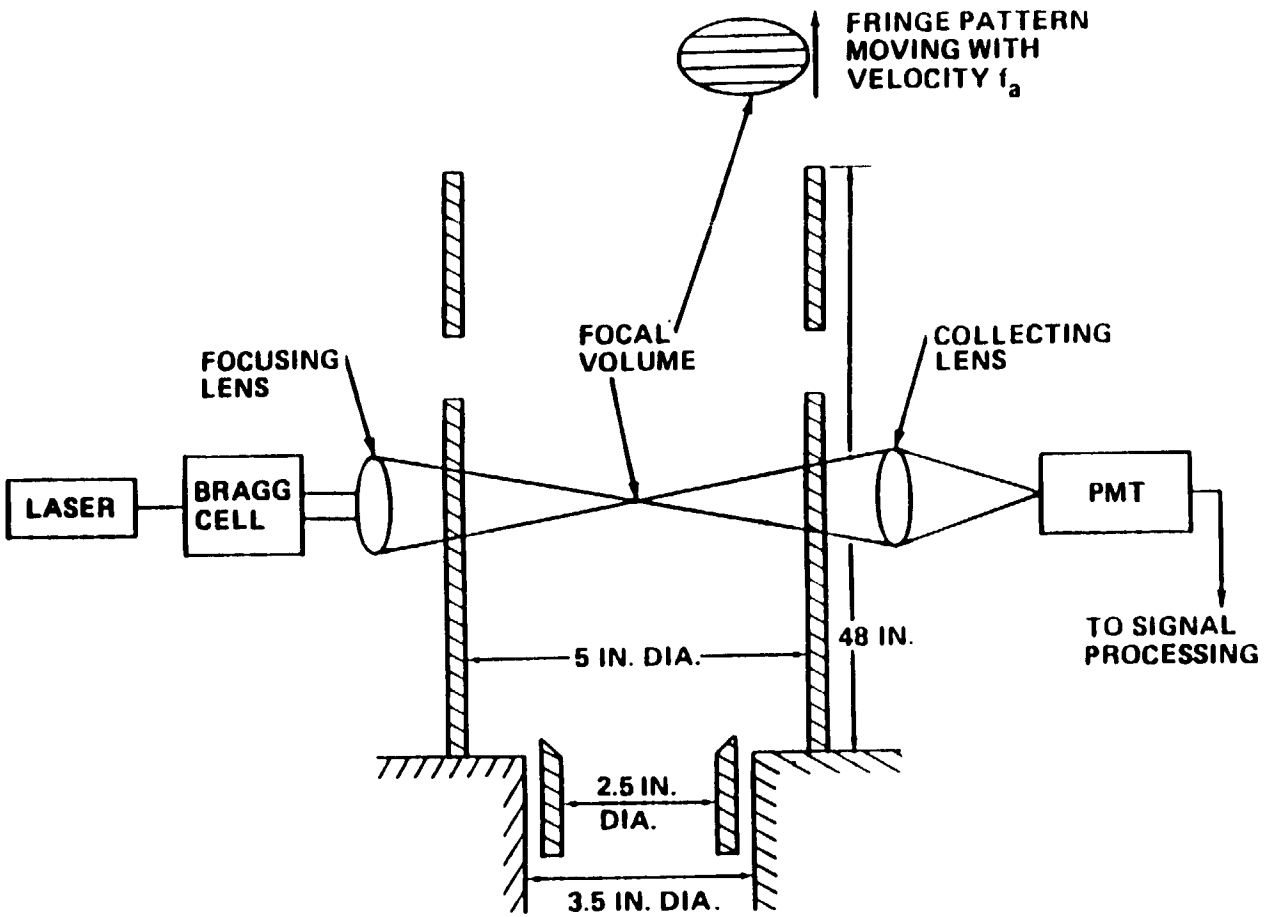

Figure 5.19 Schematic of the Confined Coaxial Jet Flow Experiment of Owen

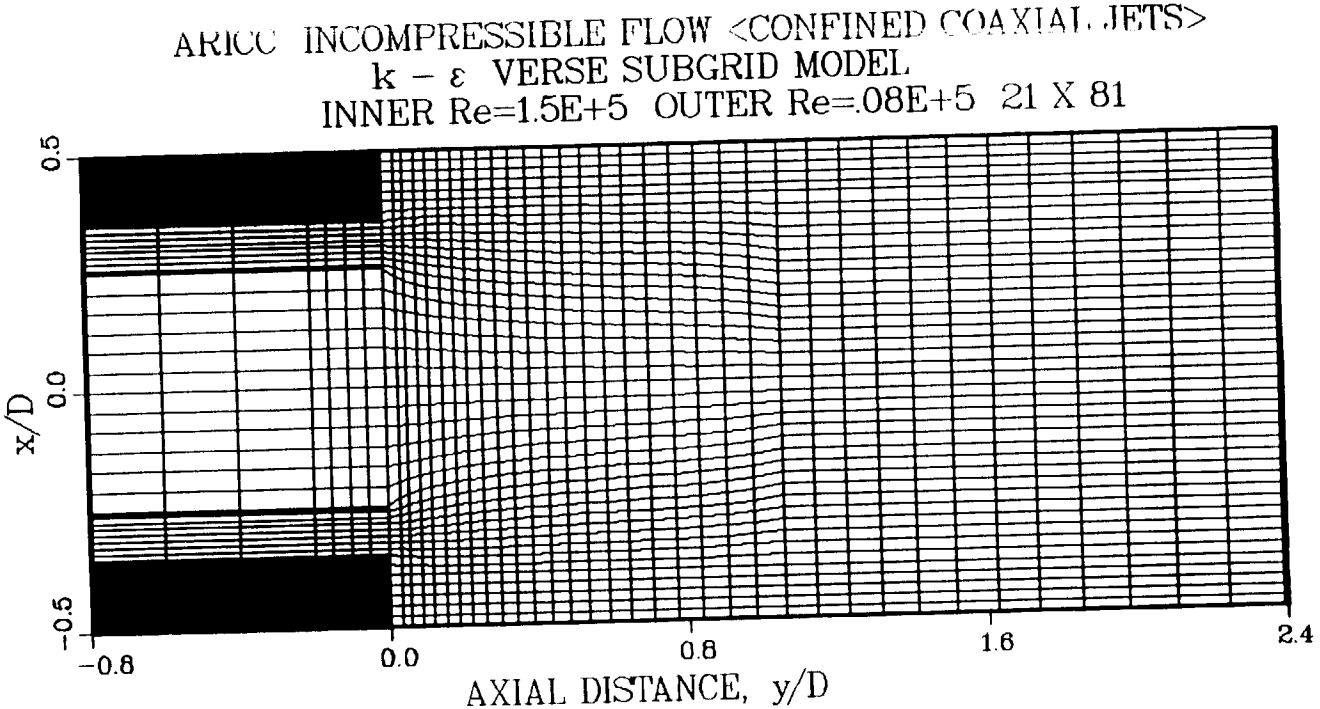

Figure 5.20 Unstructure Grid for Confined Coaxial Jet Flow

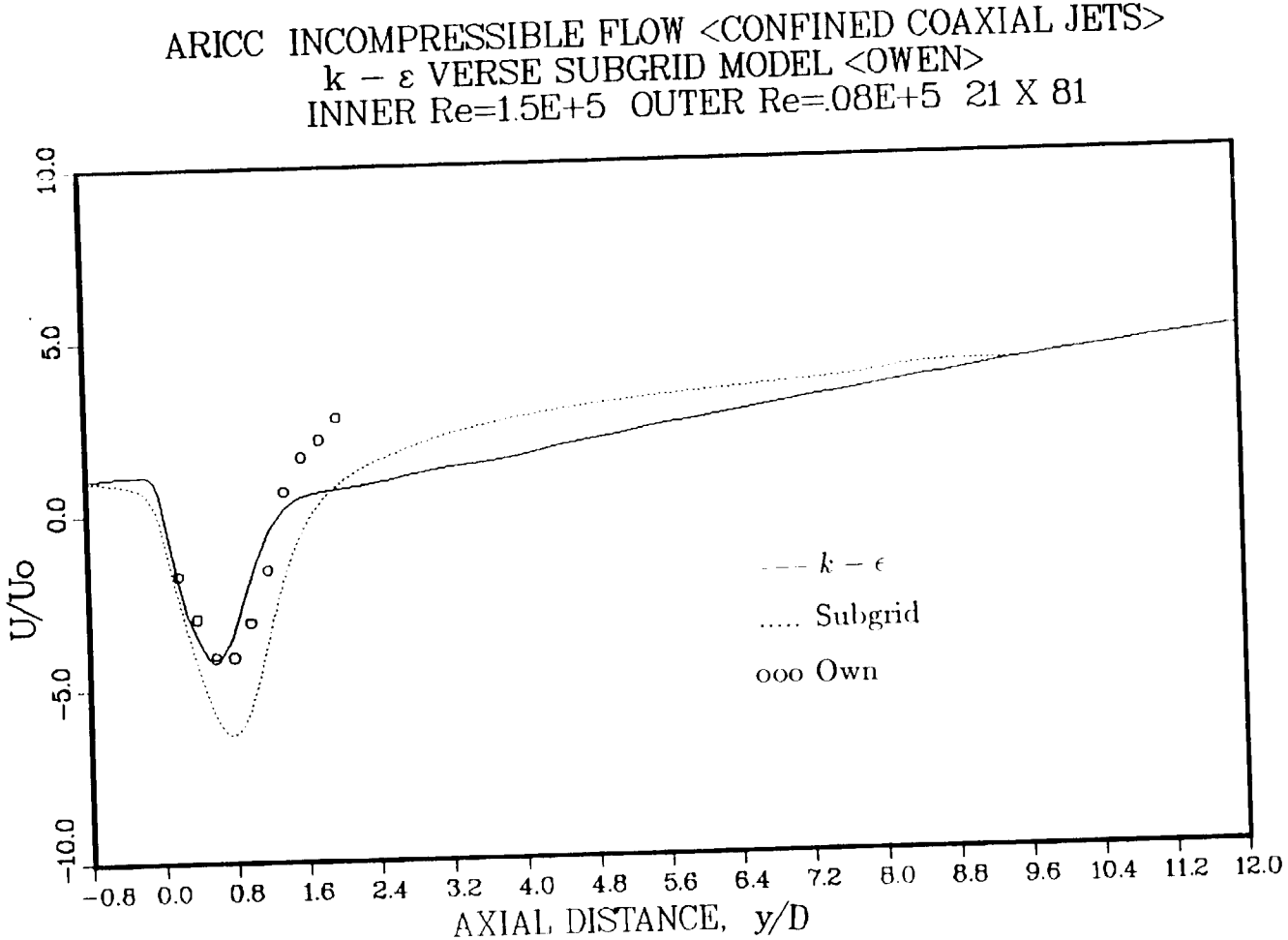

Figure 5.21 Axial Mean Velocity along the Centerline

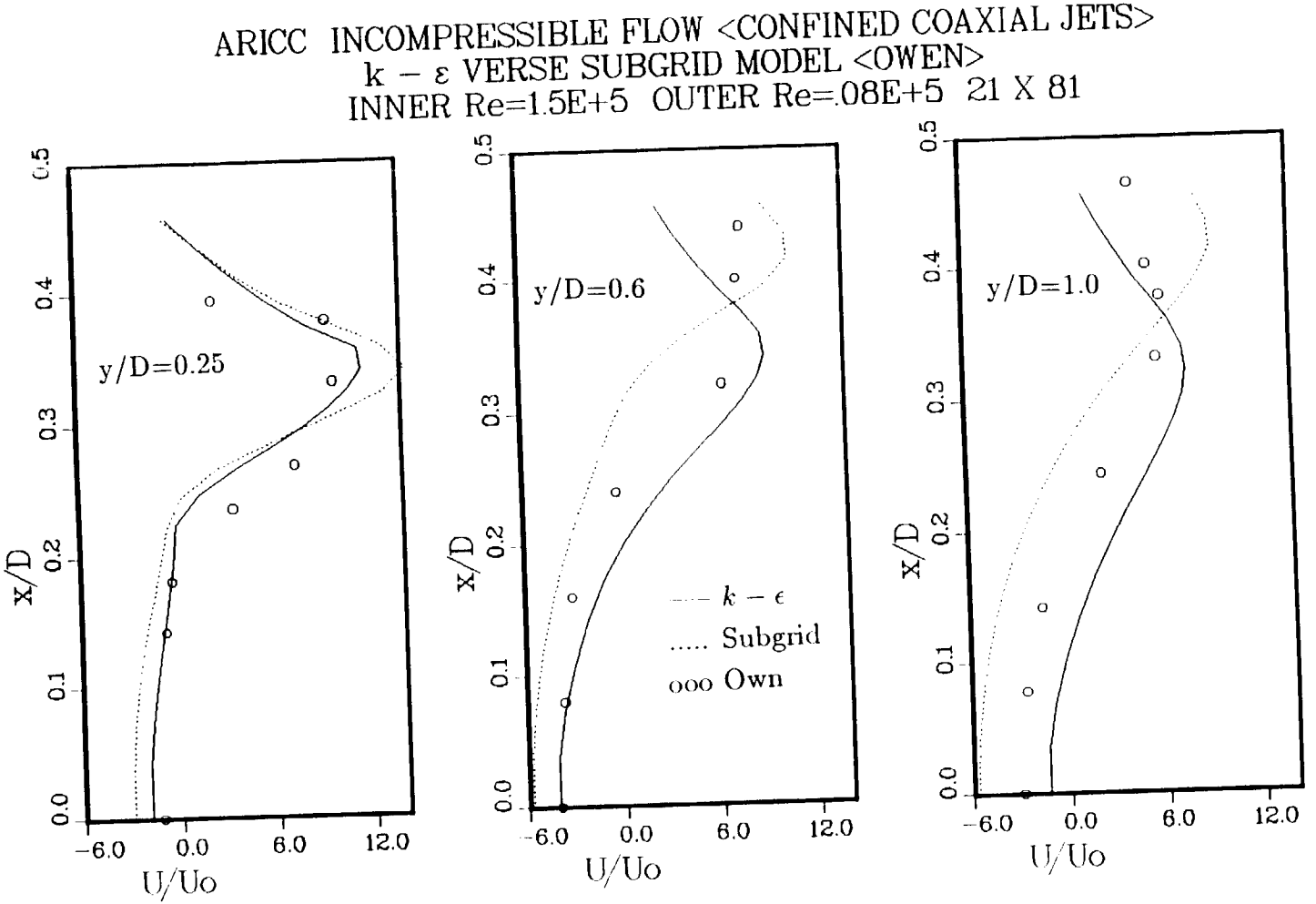

Figure 5.22 Axial Velocity at y/D=0.25, 0.6, 1.0

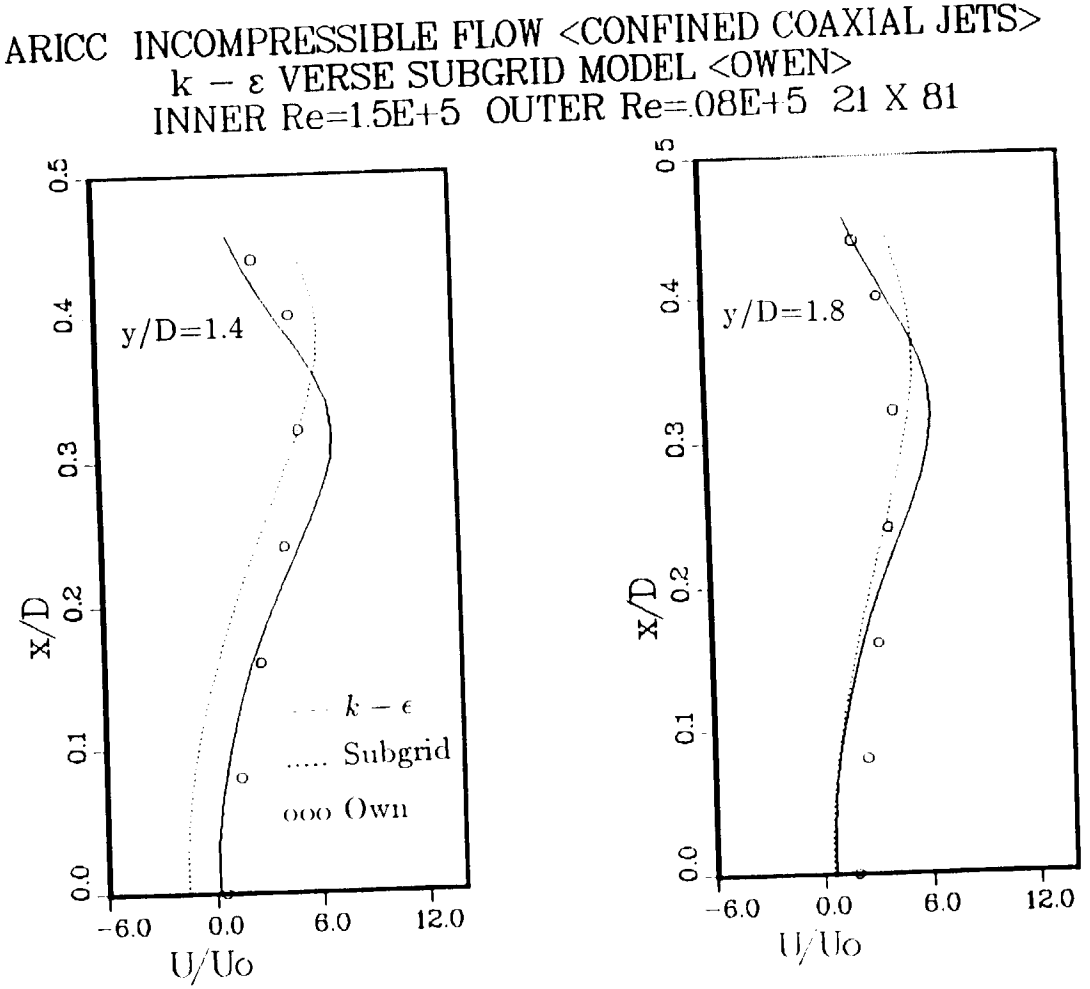

Figure 5.23 Axial Velocity at y/D=1.4, 1.8

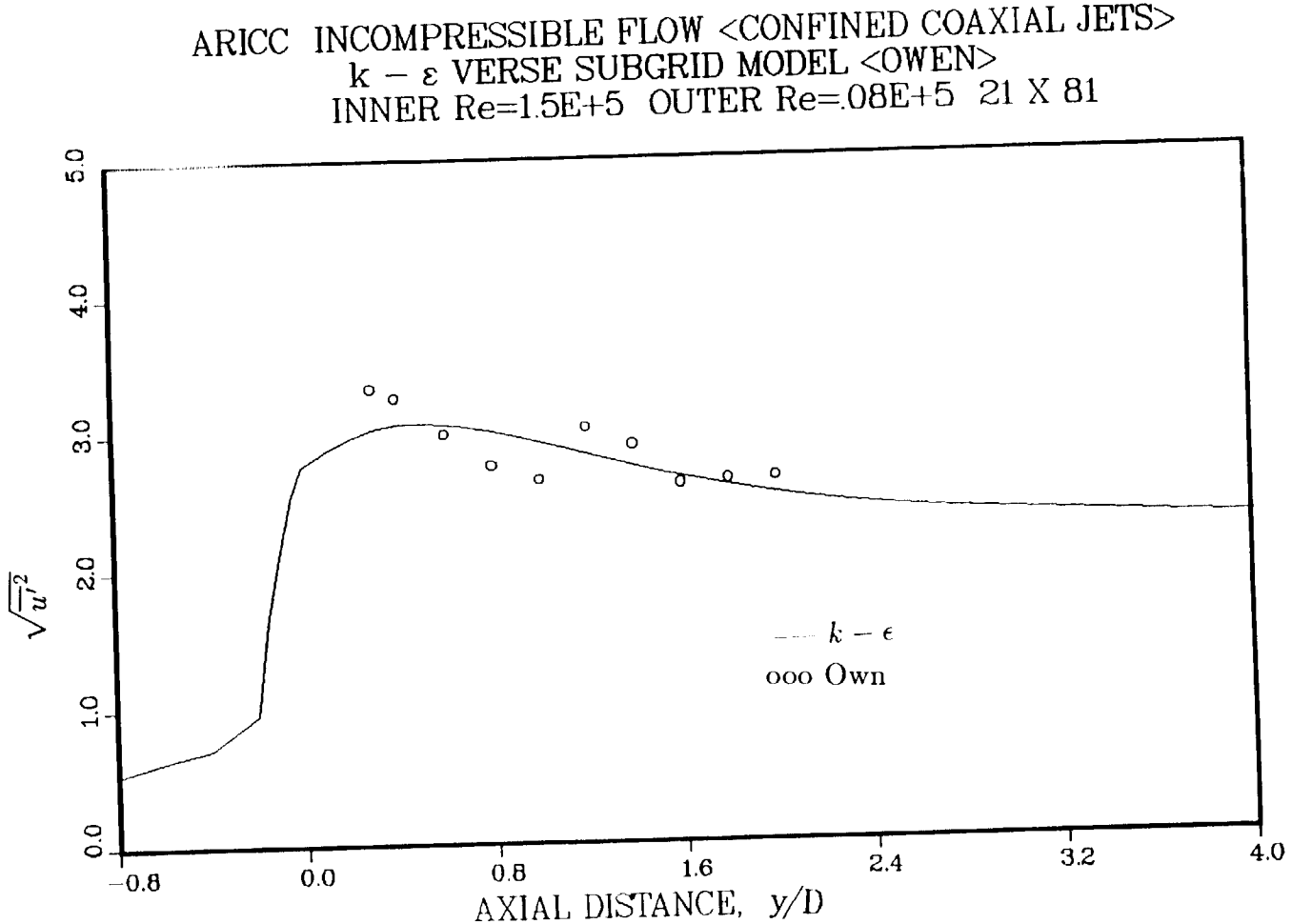

Figure 5.24 Axial Turbulence Intensity on the Centerline

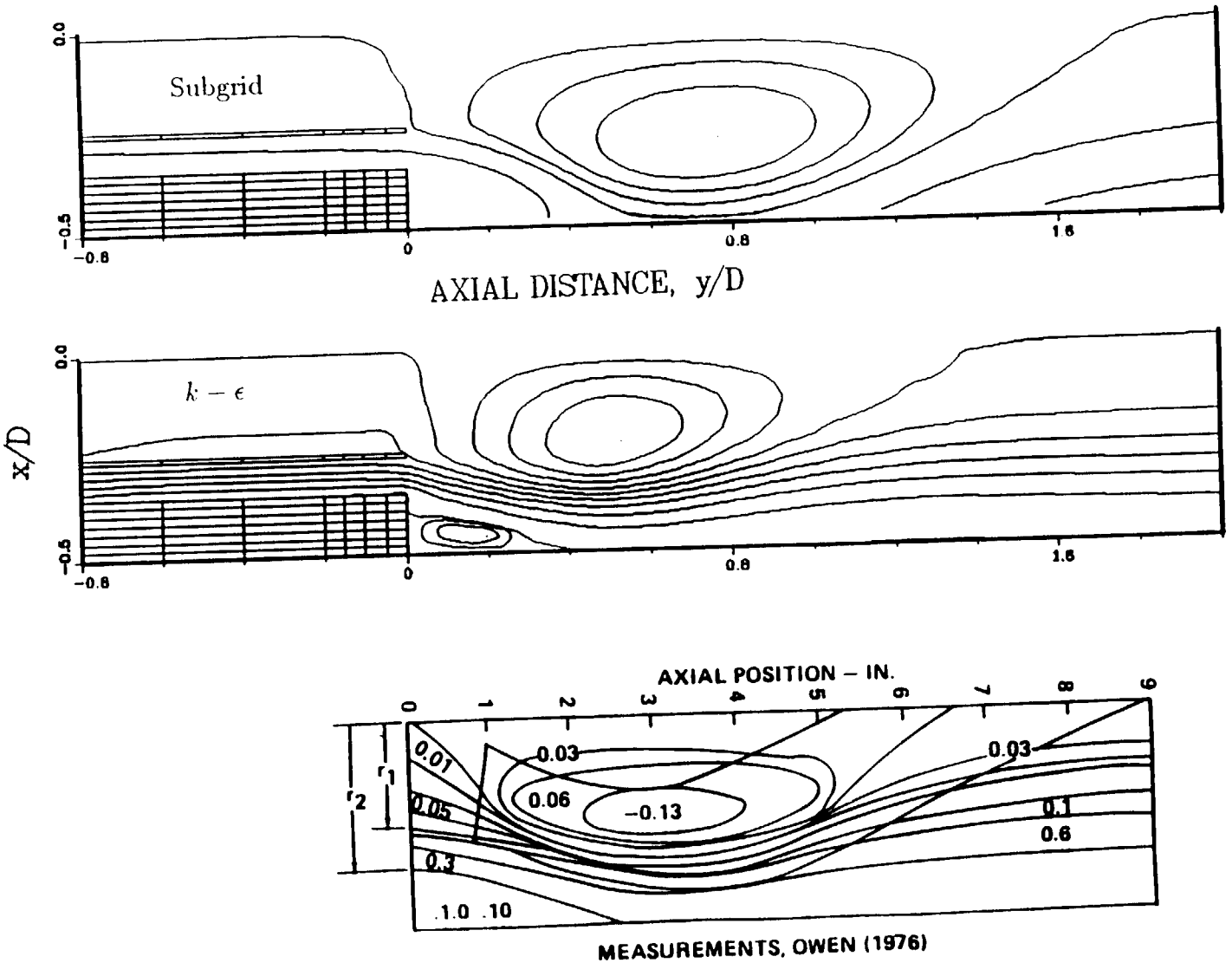

Figure 5.25 Streamline Contour vs Experiment flow Pattern

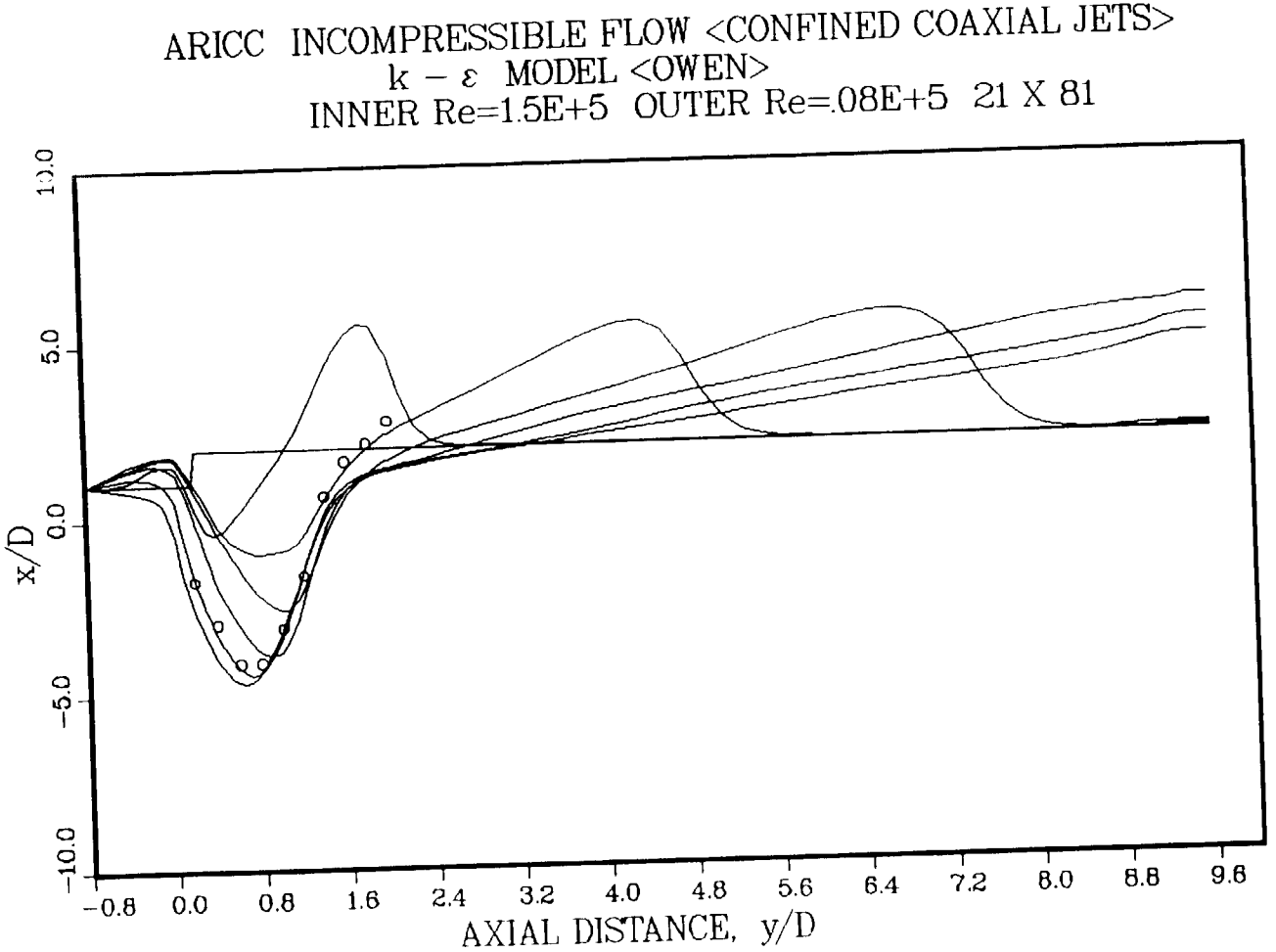

Figure 5.26 Transient Data for Confined Coaxial Jet Flow used ARICC

CHAPTER VI CONCLUSION

In this study, the ALE-ICE scheme has been applied to four different case, the Burger's equations were solved on a complex geometries with different boundary conditions. Fully Navier-Stokes equations were solved in other cases. The pseudo-compressibility method was used to solve incompressible fluid flow problems. Both laminar and turbulent pipe flows were tested and compared with the analytical solution (Bird et al. 1960) and experimental data and other predictions (Martinuzzi et al. 1989). Lastly, a confined coaxial jets flow with larger momentum difference between inner jet and annular jet were calculated. Owen's experimental data was chosen for comparison.

Results obtained from solutions of the Burger's equation by unstructured grid showed that the total r.m.s. errors, defined by equation (5.4), reached asymptotic values of 7%. Effects of viscosity on the calculated results were studied. As expected, as Reynolds numbers increase (ν decrease), convection term dominates and the total r.m.s. errors increase. For areas closed to non-orthogonal grids and Neumann B.C., there appear to have less accurate results. This points to the further development in terms of flux calculations in the ALE-ICE method for irregular grids and Neumann Boundary condition implementations. Results from laminar pipe flow showed good agreement with the analytical solution (Bird et al. 1960).

From turbulent pipe flows results, the calculations using the $k-\epsilon$ model showed good predictions except the near wall region. the discrepancies were traced to the usage of the 1/7th law wall function in which the fully developed assumptions were used. For the confined coaxial jet case, the subgrid model can not matched Owen's experimental data (1976). on the other hand, the $k-\epsilon$ model gave the closer predictions compared to the experimental data. For these tests, the adiabatic sound speed factor, $\beta = \rho c^2$, for the pseudocompressible continuity equation can not be obtained easily. The number of β suggested by Nichols et al. (1980), Anderson et al. (1984), Soh (1987) and Rogers (1987) could not be used in ARICC due to the different numerical method. Liang (1985) suggested that β could be any suitably large number to convert the small volume changes into appropriately large pressure changes. However, the $\beta's$ being used in laminar pipe flows were found to be different from those of the turbulent pipe flows. Also, the β value used in the subgrid model calculations was different with those used in the $k-\epsilon$ model calculations. It is concluded that there is no specific β that can be used in any cases. Trial and error has to be executed for each different cases. From this point of view, the pseudocompressibility method is more difficult for general fluid flow simulations.

From the results of confined coaxial jet calculations (Figure 5.27), the transient behaviors of the pseudocompressibility method in the ARICC code were not time-accurate. Those profiles look like a temporary acoustic waves pushing through the calculation domain. It is similar to the compressible flows calculations. Therefore, the ARICC code is not capable of time-accurate predictions of the liquid jet in two-phase confined coaxial jet simulations. In this regard, a subiteration scheme

can be incorporated in pseudotime to satisfy the continuity equation at each time step as done recently by Rogers and Kwak (1990).

From the cases tested in this study, it is also concluded that the ARICC code using the pointwise SOR solver is not efficient for fine grid calculations. A more efficient solver such as the conjugate gradient method should be implemented for the future usage. As for the turbulence models, the more elaborated $k-\epsilon$ model generally gave more satisfactory predictions in the cases tested compared to the subgrid model. The implementation of the 1/7th law wall function for the near wall velocity profiles was found to be inaccurate for developing flows. Further improvements on the near wall treatments of turbulence models are definitely needed.

REFERENCES

Amsden, A. A., O'Rourke, P. J., and Butler, T. D., (1989). KIVA-II: A Computer Program for Chemically Reactive Flows with Sprays, *Los Alamos National Laboratory Report LA-11560-MS.*

Anderson, D. A., Tannehill, J. C., and Pletcher, R. H., (1984). Computational Fluid Mechanics and Heat Transfer, *Hemisphere Publishing Corporation.*

Bird, R. B., Stewart, W. E, and Lightfoot, E. N., (1960). Transport Phenomena, *Wiley and Sons.*

Chorin, A. J. (1967). A Numerical Method for Solving Incompressible Viscous Flow Problems, *Journal of Computational Physics.*, vol. 2, 12.

Cloutman, L. D., Dukuwicz, J. K., Ramshaw, J. D. and Amsden, A. A., (1982). CONCHAS-SPRAY: A Computer Code for Reactive Flows with Fuel Sprays, *Los Alamos National Laboratory Report LA-9294-MS.*

Deardorff, J. W., (1970). A Numerical Study of Three-dimensional Turbulent Channel Flow at Large Reynolds Numbers, *Journal of Fluid Mechanical.*, vol. 41, 453.

Deardorff, J. W., (1971). On the Magnitude of the Subgrid Scale Eddy Coefficient, *Journal of Computational Physics.*, vol. 7.

Dukowicz, J. K., (1980) *Journal of Computational Physics.*, vol. 35, 229.

Harlow, F. H. and Amsden, A. A., (1968) *Journal of Computational Physics.* vol 3, 80.

Harlow, F. H. and Amsden, A. A., (1971) *Journal of Computational Physics.* vol 8, 197.

Hirt, C. W., Amsden, A. A. and Cook, J. L., (1974) *Journal of Computational Physics.*, vol 14, 227.

Jones, W. P. and Launder, B. E., (1972). The Prediction of Laminarization with a Two-Equation Model of Turbulence, *International Journal of Heat and Mass Transfer*, vol. 15, 1023.

Launder, D. E. and Spalding, D. B., (1974). The Numerical Computation of Turbulent Flows, *Computer Methods in Applied Mechanics and Engineering.*, vol 3, 269.

Lawn, C. J., (1971). Rate of Dissipation in Turbulent Pipe Flow, *Journal of Fluid Mechanics*, vol 48, 477.

Lee, C. M., Chen C. P., (1989). Solution of Burger's Equation in Complex Geometries and Boundaries, *Proceeding of Computational Fluid Dynamics Workshop*, The University of Alabama in Huntsville, Feb. 23, 1989.

Liang, P. Y., (1984). ARICC User's Manual.

Liang, P. Y., Fisher, S. and Chang, Y. M., (1985). Comprehensive Modeling of a Liquid Rocket Combustion Chamber. *AIAA-85-0232.*

Liang, P. Y., Jensen, R. J. and Chang, Y. M., (1986a). Numerical Analysis of SSME Preburner Injector Atomization and Combustion Processes. *AIAA-86-0454.*

Liang, P. Y., (1986b). Analysis of Coaxial Spray Combustion Flames and Related

Numerical Issues. *AIAA-86-1511.*

Lilly, D. K., (1967). *Proceedings of the IBM Scientific Computing Symposium on Environmental Sciences* IBM Form no. 320-1951, 195.

Martinuzzi, R., and Pollard, A., (1989). Comparative Study of Turbulence Models in Predicting Turbulent Pipe Flow, Part I: Algebraic Stress and $k-\epsilon$ Models, *AIAA Journal*, vol 27, 29.

Nallasamy, M., (1987). Prediction of Recirculation Zones in Isothermal Coaxial Jet Flows Relevant to Combustors, *NASA Contractor Report 4064.*

Nichols, B. D., Hirt, C. W., and Hotchkiss, R. S., (1980). SOLA-VOF: A Solution Algorithm for Transient Fluid Flow with Multiple Free Boundaries, *Los Alamos Scientific Laboratory report LA-8355.*

Nikuradse, J., (1932). Gesetzmäßigkeit der turbulenten Strömung glatten Rohen, *Verein Deutscher Ingenieure-Forschungsheft*, 356.

Novic, A. S., Miles, G. A., and Lilley, D. G., (1979). Numerical Simulation of Combustor Flow Fields: A Primitive Variable Design Capability. *Journal of Energy*, vol. 3, 95.

Owen, F. K., (1976). Measurements and Observations of Turbulent Recirculating Jet Flows, *AIAA Journal*, 14, 11, 1556.

Pracht, W. E., (1975) *Journal of Computational Physics.*, vol 17, 132.

Richman, J. W. and Azad, R. S., (1973). Developing Turbulent Flow in a Smooth Pipe, *Application Science resource*, vol 28, 419.

Rodi, W., (1975). A Review of Experimental Data of Uniform Density Free Turbulent Boundary Layers, *Studies in Convection: Theory, Measurement, and*

Applications, vol. 1, (B. E. Launder, ed.), Academic, New York.

Rogers, S. E. and Kwak, D., (1990). Upwind Differencing Scheme for the Time-Accurate Incompressible Navier-Stokes Equations", *AIAA Journal*, vol. 28, 253.

Rogers, S. E., Kwak, D., and Chang, J. L. C., (1987). INS3D-An Incompressible Navier-Stokes Code in Generalized Three-Dimensional Coordinates, *NASA Technical Memorandum 100012*

Rubesin, M. W., (1977). Numerical Turbulence Modeling, *AGARD Lecture Series No. 86 on Computational Fluid Dynamics*, 3-1.

Soh, W. Y., (1987). Time-Marching Solution of Incompressible Navier- Stokes Equations for Internal Flow, *Journal of Computational Physics*, vol 70, 232.

Sturgess, G. J., Syed, S. A. and McManus, K. R., (1983). Importance of Inlet Boundary Conditions for Numerical Simulation of Combustor Flows, AIAA-83-1263

Sysed, S. A. and Sturgess, G. A., (1980). Validation Studies of Turbulence and Models for Aircraft Gas Turbine Combustors, *In: Momentum Combustion and Heat Transfer Process in recirculating Flows*, HTD-Vol. 13, 1980, 71.